Journal of Oceanography
https://doi.org/10.1007/s10872-024-00728-6

ORIGINAL ARTICLE

Disentangling mechanisms behind emerged sea surface temperature anomalies in Indonesian seas during El Niño years: insights from closed heat budget analysis

Faisal Amri[1] · Ahmed Eladawy[1] · Joko Prihantono[2] · Takashi Nakamura[1]

Received: 28 December 2023 / Revised: 14 June 2024 / Accepted: 8 July 2024

Abstract

A surface layer (upper 20 m depth) heat budget analysis, derived from a hindcast regional-scale ocean modeling experiment, was employed to examine the underlying mechanisms behind the emergence of sea surface temperature anomalies (SSTA) in the Indonesian seas during El Niño events over the 1995–2019 course. Prior to the emergence of warm SSTA, which typically appeared following the mature phase of El Niño and lasted for almost a year, apparent anomalous heat accumulation occurred for at least 2–4 months and peaked in conjunction with the climatic event. Further examination revealed possible east–west distinct dynamics in the heat budget variations within the region during El Niño years. The anomalous heat accumulation in the western part of Indonesian seas (Java Sea) was predominantly caused by modulation in the surface net heat flux. Whereas in the eastern part (Banda Sea), the ocean circulation also exerted important influence in addition to the surface net heat flux. The ocean circulation in the eastern Indonesian seas notably contributed to moderate the effect of surface net heat flux during El Niño growth. Moreover, the same ocean circulation was responsible for prolonging the anomalous heat accumulation in the eastern Indonesian seas from mature to decay phase of the El Niño, ultimately resulted in warmer SSTA than that in the western part. The study conducted here provides additional insights on how the Indonesian seas responded to the El Niño and further reaffirms the idea that the climatic event results in anomalous warming across the Indonesian seas.

Keywords Indonesian seas · El Niño · Ocean modeling · Sea surface temperature · Heat budget analysis

1 Introduction

The Indonesian seas, situated between the Indian and Pacific Oceans, is uniquely positioned for direct impacts by the Indian Ocean Dipole (IOD) in the tropical Indian Ocean (Saji et al. 1999) and El Niño-Southern Oscillation (ENSO) in the tropical Pacific Ocean (Trenberth 1997). Various studies have addressed the response of oceanographic features in Indonesian seas to the Indo-Pacific climatic forcing (e.g., Gordon and Susanto 2001; Ningsih et al. 2013; Pujiana et al. 2019), as well as the weather pattern in the region (e.g., Hendon 2003; Giannini et al. 2007; Alsepan and Minobe 2020) and confirmed the existence of ENSO/IOD-related modulation at a certain statistical significance level. An inter-basin heat exchange between the Indian Ocean and Pacific Ocean was also inferred from both observations (Wijffels and Meyers 2004) and modeling (Zhang et al. 2018) owing to the existence of Indonesian throughflow (ITF; Gordon et al. 1999; 2019) that passes mainly through the eastern part of the Indonesian seas. All these findings on the oceanographic and weather features of the Indonesian seas, along with their modulations, have steadily gained international scientific community interest about the importance of Indonesian seas to the climate dynamics in regional-to-global scales (Sprintall et al. 2019).

The advancements in our understanding about the Indonesian seas were partly due to the improved ocean observation system (e.g., Moltmann et al. 2019) and gap-filling method (e.g., Ahn and Lee 2022) which ultimately led to refined representation of the Indonesian seas in gridded data products.

✉ Faisal Amri
faisal.amri.os12@gmail.com

[1] Transdisciplinary Science and Engineering Department, School of Environment and Society, Tokyo Institute of Technology, Ookayama 2-12-1 W8-13, Meguro, Tokyo 152-8552, Japan

[2] Research Center for Conservation of Marine and Inland Water Resources, National Research and Innovation Agency (BRIN), Cibinong 16911, Indonesia

Published online: 28 July 2024

For instance, high-resolution sea surface temperature (SST) reconstruction products (e.g., Tomita et al. 2019; Huang et al. 2021) have allowed the evaluation of long-term warming trends in SST across the region and how Indo-Pacific climatic forcings affected the secular trend (e.g., Iskandar et al. 2020). In their study, Iskandar et al. (2020) suggested the role of the ENSO warm phase (El Niño) and cool phase (La Niña) in alleviating and corroborating the warming trend in Indonesian seas, respectively. This was based on the statistically significant anti-correlation they found between the sea surface temperature anomaly (SSTA) in the area and central–eastern tropical Pacific. One of the presumed mechanisms was the horizontal advection which brings the cooler-than-usual and warmer-than-usual sea surface temperature from the western Pacific into the Indonesian seas during the El Niño and La Niña, respectively. Similarly, the positive and negative phases of IOD (pIOD and nIOD, respectively) that associated with cooler-than-usual SST and warmer-than-usual SST in some parts of the Indonesian seas that in proximity to the Indian Ocean, respectively, also suggested to affect the overall warming trend.

During El Niño years, the SSTA in the western Pacific, where the Indonesian seas are situated, (Fig. 1) can be characterized into three stages following the phases exhibited by the El Niño itself (Timmermann et al. 2018). First, the anomalous cool SSTA appeared during the growth phase of El Niño which typically took place during May–September. An apparent warm SSTA further emerged within the Indonesian seas between November and March of the succeeding year, especially in its western part, in conjunction with the El Niño mature phase. The anomalous warm SSTA became even more robust during the May–September during the year of El Niño demise.

In addition to the aforementioned SSTA pattern, anomalous descending branch of walker cell also took place during El Niño years in the western Pacific, which further affected the air–sea heat exchange and ultimately led to heat budget variations in the sea surface (Alexander et al. 2002). An earlier study on the heat budget in Indonesian seas focusing on El Niño years found that the anomalous surface heat flux played major role in controlling SSTA (Hendon 2003). The potentially overlooked effects from the influence of ocean dynamics on the heat budget were acknowledged considering the simplified surface layer heat budget analysis used in the study. Hence, emphasizing the need for a complete heat budget analysis.

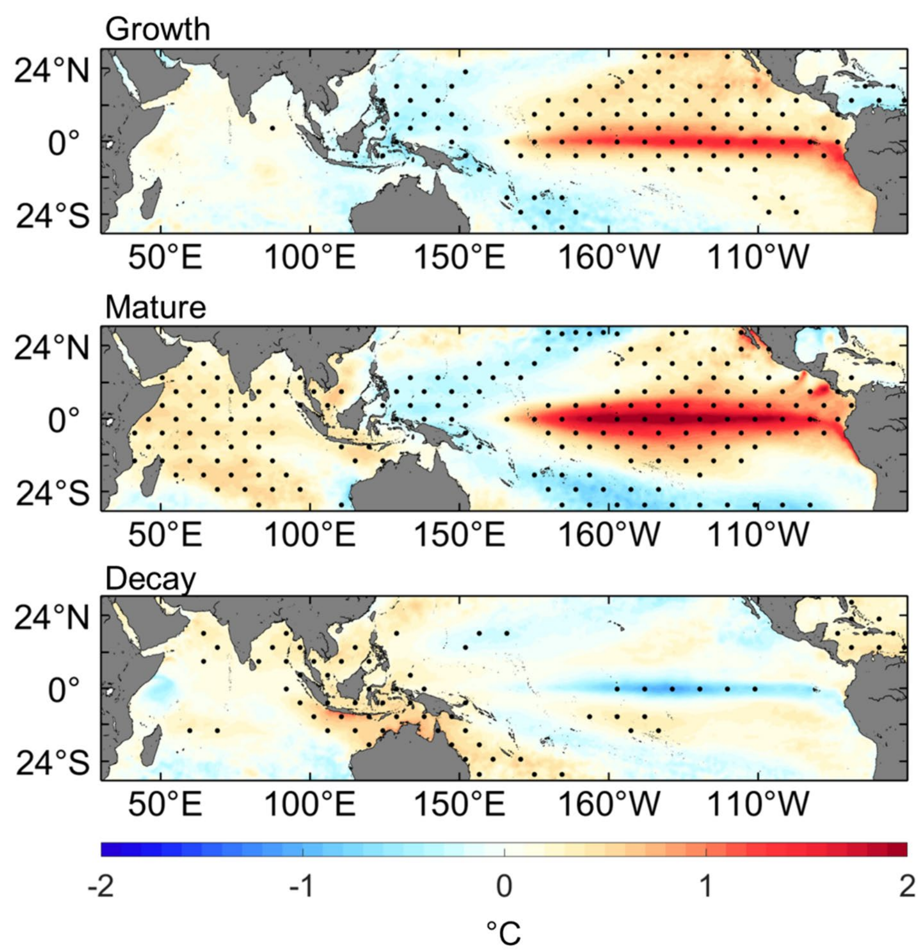

Fig. 1 Sea surface temperature anomalies (SSTA; in °C) composite average during three El Niño phases including growth (upper panel), mature (middle panel), and decay (lower panel) across the Indo-Pacific ocean according to the third version of Japanese Ocean Flux Data Sets with Use of Remote Sensing Observations (J-OFURO3; Tomita et al. 2019). Five El Niño events were selected for the composite analysis (1997/98, 2002/03, 2004/05, 2009/10, and 2015/16). Stippling indicates region with statistically significant composite SSTA ($p < 0.01$) according to the two-tailed Student's *t*-test

The exact balance between the atmospheric (i.e., air–sea heat flux) and oceanic (e.g., advection and mixing) processes which dictates the SST variations in the Indonesian seas during the El Niño events, has not been thoroughly explored. Recent attempts on heat budget analysis in the region still leave a considerable amount of residual signal, hindering a holistic interpretation (Iskandar et al. 2020; Ismail et al. 2023). Employing a numerical ocean model for heat budget analysis on the other hand, is arguably more preferable rather than utilizing publicly available observations and/or monthly oceanic reanalysis products since the budget closure can be achieved (Hasson et al. 2013; Murata et al. 2020). The utilization of oceanic models to address the complete surface layer heat budget interannual variability in the Indonesian seas can be traced back to the study by Halkides et al. (2011); however, they focused on general variability rather than specifically addressing the modulation during any El Niño event. Moreover, representing the Indonesian seas using basin-wide heat budget analysis (e.g., Halkides et al. 2011; Kida and Wijffels 2012) might overlook the localized dynamics in sea surface temperature variations (Giannini et al. 2007).

The advantage of conducting a complete heat budget analysis from an ocean modeling experiment for examining the Indonesian seas SSTA under specific anomalous climate was demonstrated by Delman et al. (2018). Focusing on pIOD events, they revealed the role of remote wind stress anomalies from west of Sumatra in driving anomalous cool SSTA in the south of Java through advection process during the onset of pIOD. The study highlighted that oceanic processes could become a main driver of SSTA, overcoming the influence from heat flux at the surface. Moreover, the performed heat budget analysis also complemented conclusions inferred from observation-based studies related to the dynamics during pIOD (Delman et al. 2016; Horii et al. 2018).

This study henceforth focused on heat budget variability in the Indonesian seas, especially during the past El Niño years, and how it related to the emerged SSTA associated with the climatic events. Our understanding on the mechanism behind the SSTA emergence in Indonesian seas is paramount as the precipitation pattern around the region was also presumed to be regulated by its own SSTA aside from the climatic events (McBride et al. 2003). To fulfill this objective, we used a long-term (26 years) regional ocean modeling hindcast experiment, with heat budget diagnostics that computed simultaneously, configured at approximately 13 km horizontal resolution and forced by a suite of realistic datasets. These have allowed us to achieve the heat budget closure as well as its long-term variabilities in response to the perturbation in the forcing datasets, primarily the atmospheric datasets.

The remainder of this paper is organized as follows. Section 2 briefly explains the numerical model used in this study along with the heat budget formulation. Section 3 provides the results, including variability simulated by the model and how these compared to observation-based datasets over the selected period, and modulation in the surface layer heat budget along with the process-specific contribution analysis during El Niño years. Finally, Sect. 4 summarizes the findings and possible implications of this study.

2 Methodology

2.1 Model description

The model employed here was based on the Regional Ocean Modeling System version 3.7 (ROMS; Shchepetkin and McWilliams 2005). The model has been used for regional scale heat/salt budget analysis in both the Indian and Pacific Oceans (e.g., Kido et al. 2019; Murata et al. 2020). Under Boussinesq and hydrostatic assumptions, ROMS solves the primitive equations on horizontal curvilinear coordinates and terrain-following vertical *s*-coordinates. The spacing between vertical coordinates in the model was controlled by a set of stretching functions (Song and Haidvogel 1994) with user-defined parameter values. The model was configured for the Indo-Pacific region (70°E–175°E; 20°S–30°N), which encompasses the tropical eastern Indian Ocean and western Pacific Ocean, at $1/8° \times 1/8°$ horizontal resolution and 30 layers of vertical level. The bathymetry of the model was obtained from the smoothed 15 arc-second of General Bathymetric Chart of the Oceans 2022 release (GEBCO2022). The vertical stretching function and parameters were set in such a way (i.e., Theta_s = 7.0; Theta_b = 0.1; and Tcline = 200 m) to permit a higher vertical resolution near the surface. For instance, the first 10 layers from the free-surface in a water column with 4000 m depth will have average thickness of less than 10 m.

The model was forced by a suite of datasets (i.e., atmospheric reanalysis product, river discharge, sea surface salinity relaxation, and tidal forcing), which allowed the model to produce low-frequency variabilities, particularly in response to the interannually varying perturbation in the prescribed atmospheric state. The 55 year Japanese reanalysis-based dataset product JRA55-do (Suzuki et al. 2018; Tsujino et al. 2018), with native horizontal resolution of $0.5625° \times 0.5625°$ and $0.25° \times 0.25°$ for the surface forcing field and river discharge, respectively, was used for the model forcings. The JRA55-do was extensively tested for the Ocean Model Intercomparison Project phase 2 (OMIP-2) where the simulated global ocean–sea-ice states showed overall improvement compared to the previous OMIP phase (Tsujino et al. 2020). The surface forcing field used for this study includes three-hourly incoming shortwave and longwave radiation, 10 m air temperature and humidity, mean sea level pressure, rainfall, and wind speed (zonal and meridional). Whereas the JRA55-do river discharges, were provided in daily temporal resolution. A total of 12 tidal constituents from the Oregon State University TPXO global tide models (Egbert and Erofeeva 2002) as well as the level 2.5 Mellor-Yamada turbulence closure model (Mellor and Yamada 1982) were employed for simulating the vertical mixing across the modeling domain.

Air–sea heat exchange, including net longwave radiation, latent heat flux, sensible heat flux, and surface net heat flux was computed internally according to the Coupled Ocean–Atmosphere Response Experiment 3.0 algorithm (COARE3.0; Fairall et al. 2003) using the prescribed surface forcing fields and SST generated by the model. Throughout the model integration, the sea surface salinity was also relaxed toward the climatological mean from the World Ocean Atlas 2018 (Zweng et al. 2018) with a 90-days relaxation time-scale. Other aspects of the model, such as horizontal mixing configuration and air–sea momentum exchange, were configured following the protocol for large-scale, high-resolution ocean modeling (Griffies and Hallberg 2000; Griffies et al. 2016; Tsujino et al. 2020).

Lateral boundary information and initialization for the model was obtained from the oceanic reanalysis product of the European Center for Medium-Range Weather Forecast Ocean Reanalysis Product Fifth Generation (ECMWF-ORAS5; Zuo et al. 2019) which has native resolution of $0.25° \times 0.25°$. The ocean reanalysis product was validated against observation-derived datasets on a global scale and demonstrated good performance in capturing SST variability across the tropical Pacific in a study by Feng et al. (2021). A mixed radiation–nudging boundary configuration (Marchesiello et al. 2001) was applied to the passive tracers (i.e., temperature and salinity) and horizontal baroclinic velocity components (u, v) with a 360 days inflow nudging time-scale. Boundary solutions for free-surface (ζ) and horizontal barotropic velocity components ($\overline{u}, \overline{v}$) were provided according to Chapman (1985) and modified radiation condition of Flather (1976), respectively. These configurations were implemented to allow gravity wave propagation associated with the imposed tidal forcing.

Preliminary analysis of the simulation results using the above design (Amri et al. 2024) suggested that the model was sufficiently robust to reproduce the basic features of the SST seasonal cycle, as indicated by an ensemble average of high-resolution SST reconstructed products (Tomita et al. 2019). The circulation features produced by the model were also validated against available observations within the Indonesian seas (Sprintall et al. 2009), including the vertical structure of water velocity related to the ITF. The simulation experiment was conducted targeting the period from January 1, 1994 to December 31, 2019 to capture the 1997/98 and 2015/16 major El Niño events, with the first year of the model output was considered as spin-up. The archived daily average output from the simulation was further processed on a monthly basis. The anomalies produced by the model were calculated as deviations from the 1995–2019 simulated climatological averages. Additionally, simple linear trend removal was applied in this study to remove possible secular trends associated with global warming.

2.2 Closed heat budget formulation

The heat budget analysis equation in this study was derived from the advective-diffusive equation for passive tracers imposed in ROMS (Song and Haidvogel 1994). The volume-averaged water temperature changes at the surface layer, bounded by free-surface ($z = \zeta$) and an arbitrary depth for the base of surface layer ($z = -h_s$), can be obtained as

$$\frac{1}{V}\iiint_V \left(\frac{\partial T}{\partial t}\right) dV = \frac{1}{V}\left[\iint_A \left(\frac{Q_{Net}}{\rho_o C_P} + \left(-K_C \frac{\partial T}{\partial z}\right)_{-h_s}\right) dA - \iiint_V (\nabla \cdot \mathbf{V}T) dV + \iiint_V \left(A_H \nabla^2 T\right) dV\right] \quad (1)$$

$$Q_{Net} = Q_{SW} + Q_{LW} + Q_{SH} + Q_{LH} \quad (1a)$$

Equation 1 encompasses the key processes driving sea water temperature changes (left-hand side) such as surface net heat flux (right-hand side, first term), vertical diffusion at the base of the surface layer (right-hand side, second term), temperature advection (right-hand side, third term), and horizontal diffusion (right-hand side, fourth term). Surface net heat flux (Q_{Net}; in Watt m^{-2}) was calculated as a sum of incoming shortwave radiation (Q_{SW}), net longwave radiation (Q_{LW}), sensible heat flux (Q_{SH}), and latent heat flux (Q_{LH}). The convention here is that positive values, which led to surface heating, indicate downward direction for the surface net heat flux and/or its components. The penetrative shortwave radiation and vertical turbulent mixing at the base of the surface layer were implicitly incorporated into the generic form of vertical diffusion $\left(-K_C \frac{\partial T}{\partial z}\right)_{-h_s}$. The seawater specific heat capacity (C_P) and density reference (ρ_o) were set to 3985 and 1025 kg m^{-3}, respectively, for the heat budget calculation in this study. Similar to a previous study by Lee et al. (2019), the base of the surface layer for the heat budget analysis was set to a depth of approximately 20 m ($h_S = 20$), as we focused our analysis on the near-surface dynamics. The 20 m depth here was still within the range of mixed-layer depth estimated from observation in the Indonesian seas (Iskandar et al. 2020; Ismail et al. 2023).

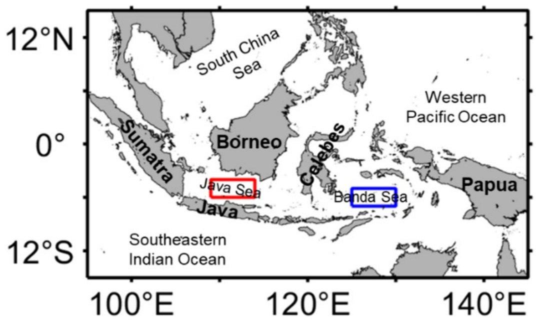

Fig. 2 Map of Indonesian seas which part of the Indo-Pacific region modeling domain. Red (106°E–114°E; 6°S–4°S) and blue (125°E–130°E; 7°S–5°S) boxes indicate the area where heat budget analysis was performed

Equation 1 was applied to two areas within the Indonesian seas that represent the western (i.e., Java Sea) and eastern parts (i.e., Banda Sea) (Fig. 2). Examination on the localized heat budget variations within the Indonesian seas under the influence of El Niño remain limited despite some findings about the different oceanographic features between the western and eastern part. For example, the two areas exhibited notable different ocean circulation pattern (Kämpf 2016; Lee et al. 2019; Liang et al. 2019) which could affect the overall temperature advection features during the El Niño years. Thus, differences on the role of advection in those areas can be expected.

The advection component of the heat budget in Eq. 1 can be reformulated according to the divergence theorem, along with the modification proposed by Lee et al. (2004)

$$\iiint_V (\nabla \cdot \mathbf{V}T)dV = \oiint_S \mathbf{V}\left(T - T_R\right) \cdot d\mathbf{S} = \oiint_S \mathbf{V}\delta T \cdot d\mathbf{S} \tag{2}$$

$$\oiint_S \mathbf{V}\delta T \cdot d\mathbf{S} = \iint \left[(u\delta T)_{East} - (u\delta T)_{West}\right]dydz + \iint \left[(v\delta T)_{North} - (v\delta T)_{South}\right]dxdz + \iint \left[(w\delta T)_{Top} - (w\delta T)_{Base}\right]dxdy \tag{2a}$$

The arbitrary non-zero temperature reference (T_R) was set as the long-term mean of volume-average temperature of each selected area in the Indonesian seas over the 1995–2019 period. The Eq. 2a redefine the volume-averaged temperature advection term into simply a net heat transport between the eastern, western, northern, southern, top, and base interfaces of water volume of interest. It should be noted that a vertical boundary condition was also applied where there was no upward heat transport through advection at the free-surface. Thus, the $\iint (w\delta T)_{\mathrm{Top}} dxdy$ term will be equal to zero. Reformulation of the temperature advection component on the heat budget analysis above allowed us to separate the influence of external process of heat transport from the outside and the internal process of heat redistribution, which can occur within the area of interest (Lee et al. 2004; Zhang et al. 2018).

Practically, the quadratic term of $\mathbf{V}\delta T$ (i.e., heat transport) in the model used here was provided as a time-averaged value such as monthly average and follows the below relationship (Wilkin 2006).

$$\langle \mathbf{V}\delta T \rangle = \langle \mathbf{V} \rangle \langle \delta T \rangle + \left\langle \mathbf{V}'\delta T' \right\rangle \tag{3}$$

where $\langle\rangle$ denotes the monthly averaged value of each corresponding variable (i.e., $\mathbf{V}\delta T$, $\mathbf{V}$, and, δT). Additionally, the $\langle \mathbf{V} \rangle \langle \delta T \rangle$ term can be further expanded using the Reynolds decomposition of $\langle \mathbf{V} \rangle = \langle \overline{\mathbf{V}} \rangle + \langle \mathbf{V}' \rangle$ and $\langle \delta T \rangle = \langle \overline{\delta T} \rangle + \langle \delta T' \rangle$ as in Lee et al. (2004). The aforementioned overbar and prime denote the climatological component and anomalies component, respectively. The first term of the right-hand-side Eq. 3 hence, can be expanded into.

$$\langle \mathbf{V} \rangle \langle \delta T \rangle = \left\langle \overline{\mathbf{V}} \right\rangle \left\langle \overline{\delta T} \right\rangle + \left\langle \overline{\mathbf{V}} \right\rangle \langle \delta T' \rangle + \langle \mathbf{V}' \rangle \left\langle \overline{\delta T} \right\rangle + \langle \mathbf{V}' \rangle \langle \delta T' \rangle \tag{3a}$$

Further applying surface integral on the Eq. 3 with expanded $\langle \mathbf{V} \rangle \langle \delta T \rangle$ as in Eq. 3a yields.

$$\oiint_S \langle \mathbf{V}\delta T \rangle \cdot d\mathbf{S} = \oiint_S \left(\langle \overline{\mathbf{V}} \rangle \langle \overline{\delta T} \rangle + \langle \overline{\mathbf{V}} \rangle \langle \delta T' \rangle + \langle \mathbf{V}' \rangle \langle \overline{\delta T} \rangle + \langle \mathbf{V}' \rangle \langle \delta T' \rangle + \langle \mathbf{V}'\delta T' \rangle \right) \cdot d\mathbf{S} \tag{3b}$$

The anomalous temperature tendency associated with the temperature advection process therefore, can be reformulated as.

$$\left[-\frac{1}{V} \oiint_S \langle \mathbf{V}\delta T \rangle \cdot d\mathbf{S} \right]' = \left[-\frac{1}{V} \oiint_S \langle \overline{\mathbf{V}} \rangle \langle \delta T' \rangle \cdot d\mathbf{S} \right]' + \left[-\frac{1}{V} \oiint_S \langle \mathbf{V}' \rangle \langle \overline{\delta T} \rangle \cdot d\mathbf{S} \right]' + \left[-\frac{1}{V} \oiint_S \langle \mathbf{V}' \rangle \langle \delta T' \rangle \cdot d\mathbf{S} \right]' + \left[-\frac{1}{V} \oiint_S \langle \mathbf{V}' \rangle \langle \delta T' \rangle \cdot d\mathbf{S} \right]' \tag{3c}$$

which for conciseness reasoning, will be written in the rest of this manuscript as following Eq. 4;

$$[\langle \mathbf{V}\delta T \rangle]' = \underbrace{\left[\langle \overline{\mathbf{V}} \rangle \langle \delta T' \rangle \right]'}_{Term1} + \underbrace{\left[\langle \mathbf{V}' \rangle \langle \overline{\delta T} \rangle \right]'}_{Term2} + \underbrace{\left[\langle \mathbf{V}' \rangle \langle \delta T' \rangle \right]'}_{Term3} + \underbrace{\left[\langle \mathbf{V}' \rangle \langle \delta T' \rangle \right]'}_{Term4} \tag{4}$$

The Eq. 4 is similar to the equation used in previous heat-budget studies (Lee et al. 2004; Feng et al. 2021). The above equation separates the temperature advection anomalies into several components related to the following processes: advection of anomalous temperature by mean flow (Term 1), advection of mean temperature by anomalous flow (Term 2), advection of anomalous temperature and by anomalous flow (Term 3), and eddy flux of temperature (Term 4).

2.3 Other datasets

Aside from the dataset used for the simulation, several observation-based datasets were employed for this study. The third version of Japanese Ocean Flux Data Sets with Use of Remote-Sensing Observations (J-OFURO3; Tomita et al. 2019) were used to validate the simulated air–sea heat exchange variability. These includes the monthly SSTA, surface net heat flux (along with its components), and surface wind stress anomalies which gridded at 0.25° × 0.25° resolution. The J-OFURO3 data is available from 1988 to 2017 with the surface wind stress variables available from 1991. We chose to use the data during the 1995–2017 period which covers the strong 1997/98 and 2015/16 El Niño events and overlapped with the simulation experiment conducted here. An additional dataset for monthly sea surface height anomaly (SSHA) was obtained from the Copernicus Climate Change Service (C3S) platform, which is a reconstruction product from various satellite missions (Sánchez-Román et al. 2023). The SSHA was found to be a good proxy for ITF variability (Pujiana et al. 2019) and ocean circulation at the surface (Chen et al. 2020). Similar to the J-OFURO3, the SSH product from C3S was also configured at native horizontal resolution of 0.25° × 0.25°. We also applied a linear trend removal for both data from J-OFURO3 and C3S.

Lastly, two climatic indices, the central–eastern tropical Pacific NINO3.4 SSTA and Indian Ocean Dipole Mode Index (DMI), were used in this study to represent the ENSO and IOD events, respectively. The climate indices were based on the monthly global SSTA reconstruction product (Rayner et al. 2003) and archived at the Physical Science Laboratory of the National Oceanic and Atmospheric Administration (PSL NOAA). The definition of El Niño years in this study followed criteria proposed by Trenberth (1997) after smoothing the NINO3.4 SSTA with 5 months moving average. The El Niño events were further determined whenever the smoothed NINO3.4 SSTA exceeded + 0.4 °C threshold for at least 6 months consecutively. According to the used threshold here, there were six El Niño years that overlapped with the model integration period (i.e., 1997/98, 2002/03, 2004/05, 2009/10, 2015/16, 2018/19). Using the similar criteria for La Niña (i.e., −0.4 °C threshold), there were also some La Niña events that succeeded the aforementioned El Niño years such as the 1998–2000 and 2010–2012 La Niña. The El Niño years classification is generally consistent with the probabilistic-approach-based ENSO index (Zhang et al. 2019).

The same data treatment as in Saji et al. (1999), which involved the removal of low-frequency signal and moving average smoothing, was applied to the DMI time-series. The DMI was firstly calculated as the SSTA difference between western Indian Ocean and southeastern tropical Indian Ocean (See Saji et al. 1999 for more details). The IOD event classification further adapted the one-standard deviation of processed DMI (± 1σ), similar to the study by Kido et al. (2019). We came up five pIOD (1997, 2006, 2015, 2018, and 2019) and four nIOD (1996, 1998, 2010, and 2016) events with two pIOD events that occurred concurrently with El Niño (i.e., 1997 and 2015). A summary of the El Niño years along with the IOD conditions over the 1995–2019 period is provided in Table 1.

3 Results and discussion

3.1 Produced variability compared to reference datasets

We first checked the simulated SSTA and SSHA spatial–temporal structure in Indonesian seas during El Niño years against the reference datasets. Here, the comparison was done based on the aforementioned El Niño phases: the growth phase in Year^0 (May^0–Sep^0), the mature phase in the transition from Year^0 to Year^{+1} (Nov^0–Mar^{+1}), and the decay phase in the succeeding year of Year^{+1} (May^{+1}–Sep^{+1}). For example, in the 1997/98 El Niño, the May^0–Sep^0 of Year^0, Nov^0–Mar^{+1} in the transition from Year^0 to Year^{+1}, and May^{+1}–Sep^{+1} of Year^{+1} periods correspond to May 1997–September 1997, November 1997–March 1998, and May 1998–September 1998, respectively. Comparison results on both SSTA and SSHA structure during El Niño years are provided in Fig. 3.

Table 1 El Niño years over the 1995–2019 period according to the NINO3.4 sea surface temperature anomalies and criteria proposed by Trenberth (1997)

El Niño years	Duration	IOD condition
1997–1998*	13 months (April 1997–April 1998)	Strong positive IOD (July 1997–February 1998)
2002–2003	9 months (June 2002–February 2003)	Neutral
2004–2005	7 months (August 2004–February 2005)	Neutral
2009–2010*	10 months (July 2009–April 2010)	Neutral
2015–2016	21 months (September 2014–May 2016)	Weak positive IOD (July 2015–November 2015)
2018–2019	10 months (September 2018–June 2019)	Strong positive IOD (August 2018–December 2019; continued until 2020)

*El Niño followed by La Niña

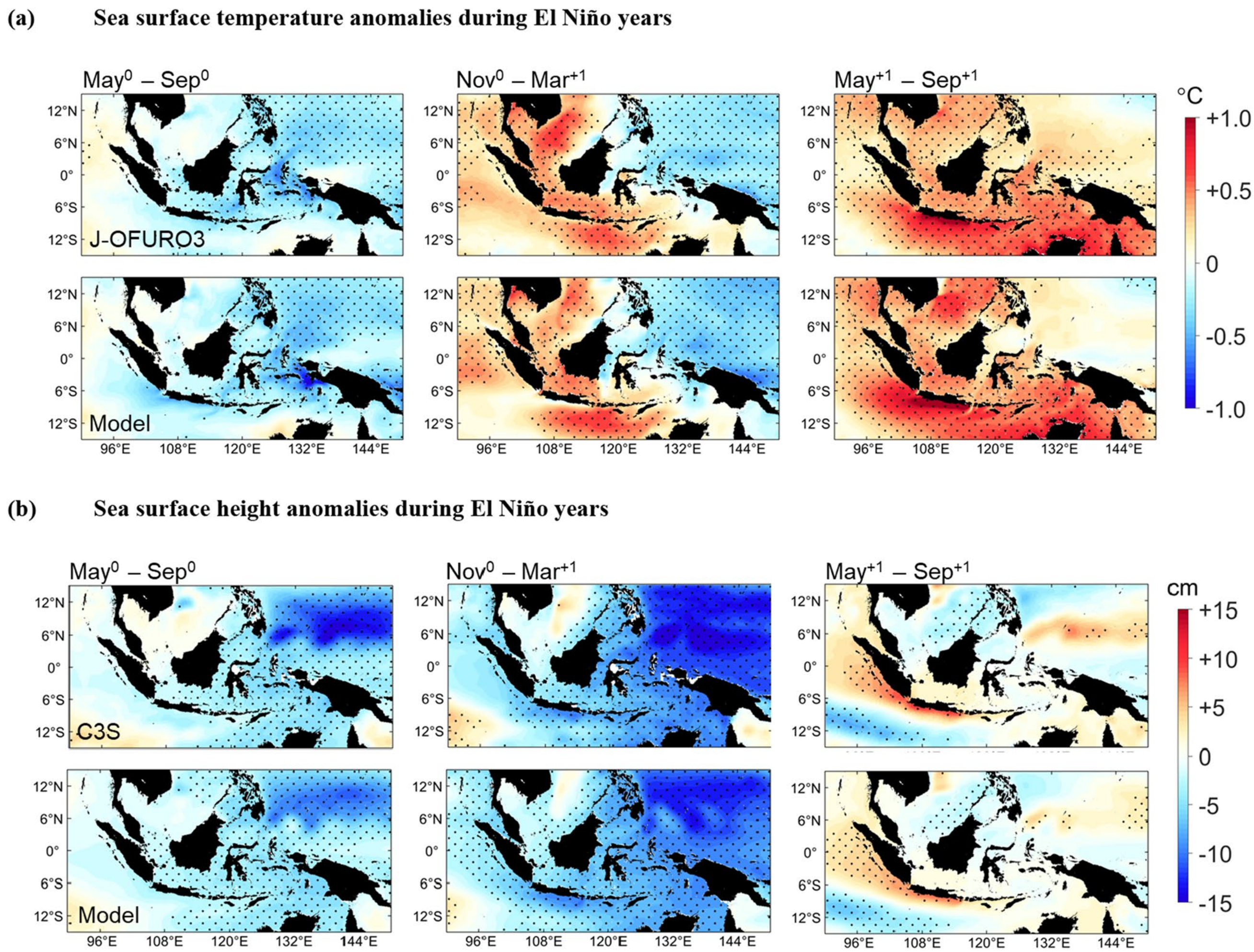

Fig. 3 Composite average of a) SSTA (in °C) and b) SSHA (in cm) across the Indonesian seas according to reference dataset (upper figures of each panel) and simulation result (bottom figures of each panel) during El Niño years over the 1995–2019 period. Stippling indicates region with statistically significant composite SSTA ($p<0.01$) according to the two-tailed Student's *t*-test

The model generally captured both SSTA and SSHA structure across the Indonesian seas during El Niño years, starting from a widespread lower-than-usual SST in May^0–Sep^0, which gradually evolved into warm SSTA in May^{+1}–Sep^{+1} (Fig. 3a). The SSH also started with lower-than-usual condition across the Indonesian seas in May^0–Sep^0 and lasted until Nov^0–Mar^{+1} before the interior part of the region showed some relaxation toward normal condition in May^{+1}–Sep^{+1} (Fig. 3b). An apparent inconsistency between the SSTA and SSHA in the region was observed from both simulation and reference datasets particularly during Nov^0–Mar^{+1} when lower-than-usual SSH was in conjunction with warm SSTA. The achieved agreement between simulation and reference datasets here further confirms the existence of underlying physics behind the emerged SSTA across the Indonesian seas.

Comparison of the produced variability further focused on the two selected areas within the Indonesian seas (Fig. 4). As previously hinted by Hendon (2003) about the influence of air–sea heat exchange, we included the air–sea heat flux and related parameters from the J-OFURO3 for this comparison. Simulated anomalies during El Niño years also agreed well with reference datasets, with the correlation coefficient ranging from 0.73 to 0.95 for the SSTA, Q_{Net} anomalies, and wind stress anomalies. Most of the air–sea heat flux component also showed consistency between the model results and J-OFURO3, denoted by an r value more than 0.65 for the Q_{SW}, Q_{LW}, and Q_{LH} anomalies. The model showed relatively poor agreement against the J-OFURO3 on the Q_{SH} anomalies component ($r=0.48$ and $r=0.16$ for western and eastern Indonesian seas, respectively). However, later analysis showed that the sensible heat flux contribution to the overall

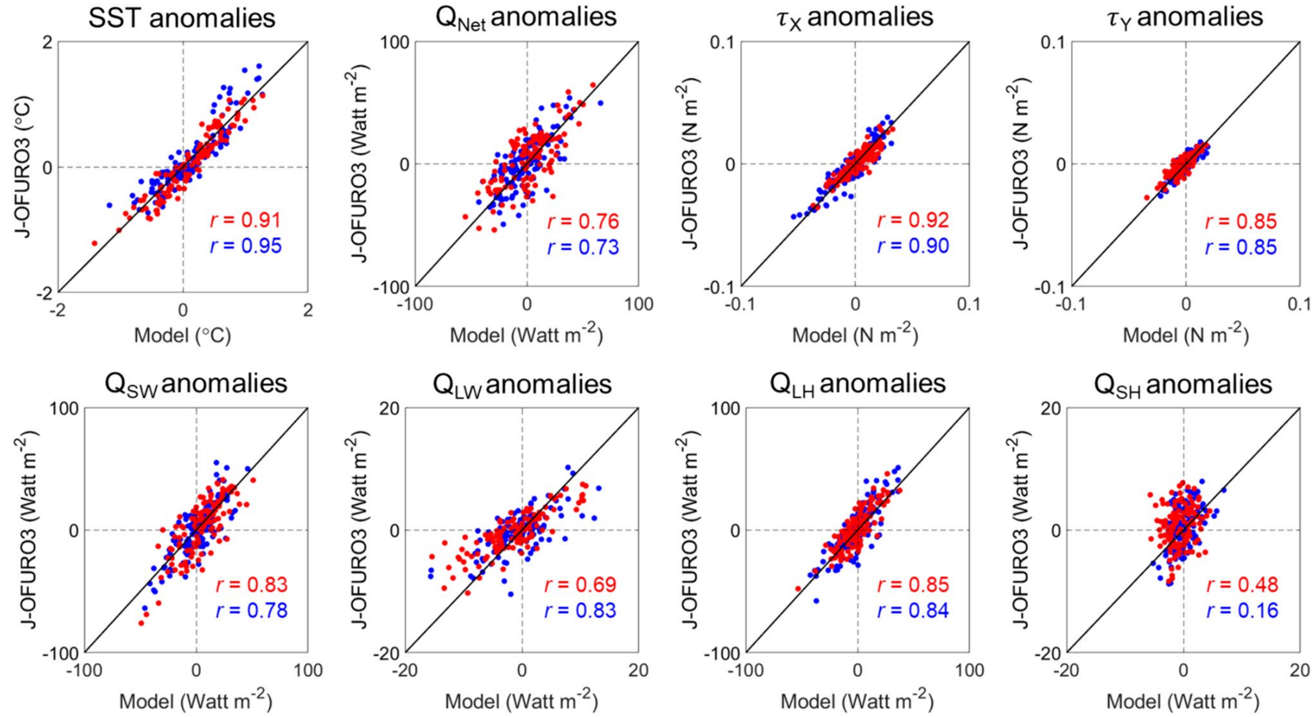

Fig. 4 Scatter plots of simulated anomalies (horizontal axis) and J-OFURO3 dataset (vertical axis) for various parameters related to the air–sea heat flux in the western (red marker) and eastern (blue marker) Indonesian seas. Q_{Net}, τ_x, τ_y, Q_{SW}, Q_{LW}, Q_{LH}, and Q_{SH} in the figure indicate the surface net heat flux, zonal surface wind stress, meridional surface wind stress, net shortwave radiation, net longwave radiation, latent heat flux, and sensible heat flux, respectively

heat budget variations was almost negligible and likely did not lead to a notable mismatch in the simulated SSTA.

The agreement achieved between simulation results and the reference dataset conducted here implies at least two things. First, the indicated SSTA structure during El Niño years across the Indonesian seas from the reconstruction product were physically robust, considering that we did not impose any data assimilation scheme on the SST during the model integration (i.e., forced run). Second, the underlying processes behind the produced SSTA in two selected areas were also realistic enough considering the general consistency in the air–sea heat exchange anomalies feature between simulated and estimated variability from the reference dataset. Some discrepancies can be attributed to both model parameterization (Kido et al. 2019) and even an error in the analysis process in the reconstruction product due to unresolved eddy-rich region (Moreton et al. 2020; Cheng 2024). Nevertheless, the comparison results here provide an initial foundation for further heat budget analysis derived from the model result.

3.2 Surface layer heat budget variability over the 1995–2019 period

A low-pass Butterworth filter with a 13 month periodicity cut-off was applied to the simulated surface layer heat budget and temperature anomalies to isolate high-frequency signals that still apparent in the monthly time-series and to retain signals with much lower frequency (i.e., interannual timescale or longer). From now on, unless stated, analyzed heat budget will be based on the low-pass filtered data between 1996 and 2018 considering the transient edge effect introduced by the low-pass filter. A partial correlation analysis on the low-pass filtered surface heat budget variations against NINO3.4 and DMI was further performed. The two climatic modes have exhibited significant correlation over the last few decades (Saji and Yamagata 2003), which implies the possibility of IOD imprinting, to some extent, on the ENSO signal (and *vice versa*) and further influenced the Indonesian seas. A similar approach was also used to partition the influence of ENSO and/or IOD on the interannual variations in weather/climate parameters around the Indonesian seas (e.g., Hendon 2003; Pujiana et al. 2019; Iskandar et al. 2020). Both climatic forcings showed significant influences ($p < 0.05$) on the overall heat budget interannual variations in the Indonesian seas, especially between October and the

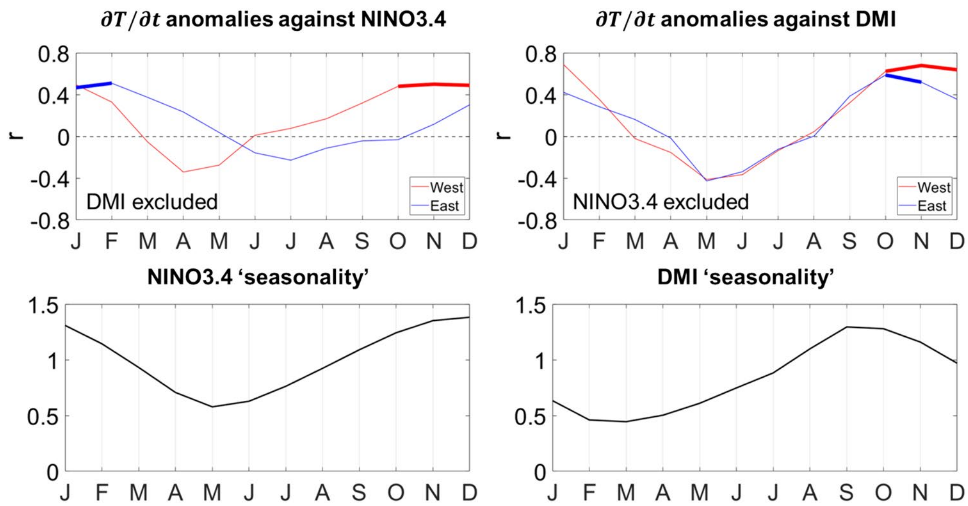

Fig. 5 (Upper panel figures) Partial correlation analysis results between surface layer temperature tendency anomalies in the Indonesian seas, represented by western (red solid line) and eastern (blue solid line) part, and Indo-Pacific climatic forcing represented by the NINO3.4 SSTA (for ENSO) and DMI (for IOD). Thicker solid line in indicates period with statistically significant correlation at $p < 0.05$ according to the two-tailed Student's *t*-test. Solid red and blue line in all figures indicate the western and eastern Indonesian seas, respectively; (Lower panel figures) monthly standard deviation value of normalized NINO3.4 and DMI which depict the typical period when the ENSO and IOD matured (hence the 'seasonality' term), respectively

succeeding February when ENSO and IOD typically peaked (Fig. 5).

In the western Indonesian seas, the average October–February correlation and correlation maximum value (r and r_{Max}, respectively) between the anomalous temperature tendency against NINO3.4 and DMI was $r = +0.46$ ($r_{Max} = +0.50$) and $r = +0.60$ ($r_{Max} = +0.69$), respectively. Whereas in the eastern part, the October–February r value was $+0.27$ ($r_{Max} = +0.51$) and $+0.43$ ($r_{Max} = +0.59$) for correlation between the temperature tendency anomalies against NINO3.4 and DMI, respectively. The number of months within the October–February in which NINO3.4 correlated with the temperature tendency anomalies at $p < 0.05$ is greater in the western (four months) than that in the eastern Indonesian seas (two months). Thus, the ENSO is closely related to the temperature tendency anomalies for at least 2–4 months within the October–February each year. Positive correlation between the temperature tendency anomalies in the Indonesian seas with both NINO3.4 and DMI during the October–February further implies that a concurrent event of El Niño and pIOD will likely result in a stronger anomalous warming tendency compared to a standalone El Niño event.

Figure 6 shows the temporal evolution of both SSTA and associated temperature tendency anomalies in the two selected areas in Indonesian seas during El Niño years according to the simulation result. Notable differences on the SSTA features during Year^0 can be observed where cool SSTA in the eastern Indonesian seas was more apparent than that in the western Indonesian seas. At the end of Year^0, in conjunction with the onset of El Niño mature phase, both areas started to shift toward an anomalous warm SSTA. The anomalous warm SSTA lasted for almost a year before getting relaxed at the end of Year^{+1}. Shifts in the SSTA during late Year^0 here were preceded by anomalous warming tendency commenced in Year^0 and peaked within the Nov^0–Mar^{+1} period in unison with the mature phase of El Niño. The warming tendency anomalies in both areas generally peaked in December of Year^0. For the extreme case of the 1997/98 El Niño, the anomalous warming tendency peak can be as high as $+0.36$ °C month^{-1} and $+0.26$ °C month^{-1} for the western and eastern Indonesian seas, respectively.

At the end of Year^{+1}, both selected areas in the Indonesian seas exhibited anomalous surface cooling tendencies together with the change in the NINO3.4 toward negative values (i.e., tendency toward La Niña-like state). On the transition from anomalous warming tendency during peak El Niño in Year^0 to cooling tendency anomalies in the end of Year^{+1}, there was a period when heat budget variations in the western Indonesian seas was restored toward normal conditions. However, in the eastern Indonesian seas, the anomalous warming tendency from peak El Niño was extended until May^{+1}–Sep^{+1} before starting to shift toward cooling tendency anomalies. The cooling tendency anomalies at the end of Year^{+1} here were likely associated with the typical El Niño cycle (Timmermann et al. 2018). This was based on only two El Niño events (1997/98, and 2009/10) that actually evolved into La Niña as per the definitions used in this study. It is known that El Niño could be a precursor for La Niña

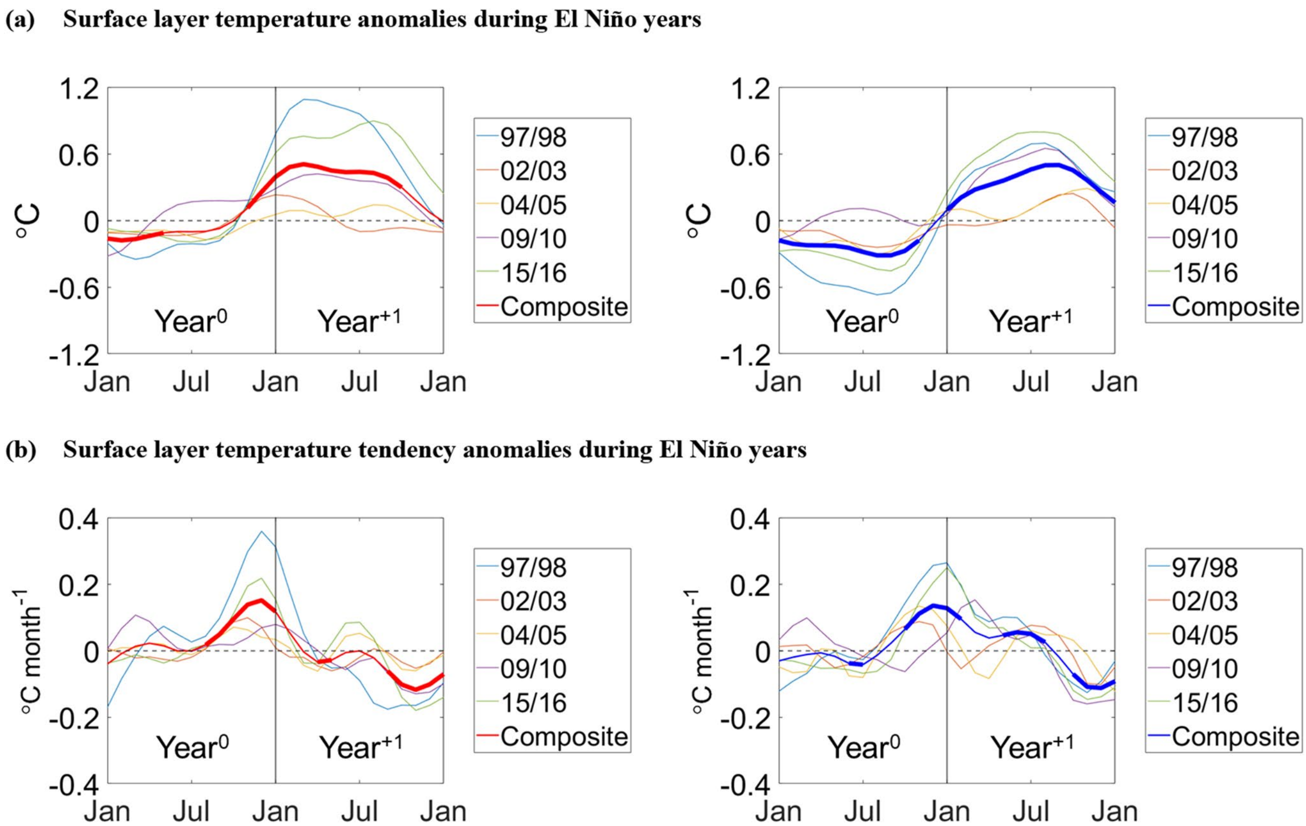

Fig. 6 Composite analysis of the sea surface **a** temperature (in °C) and its **b** tendency (in °C month^{-1}) anomalies during El Niño years in western (red solid line) and eastern (blue solid line) Indonesian seas over the 1995–2019 period. Composite analysis was set so that it encompasses the El Niño growth-to-mature (Year^{0}) and decay (Year^{+1}) period. Thicker solid red and blue line indicate periods where the composite averages were statistically significant at $p<0.1$ according to the two-tailed Student's *t*-test

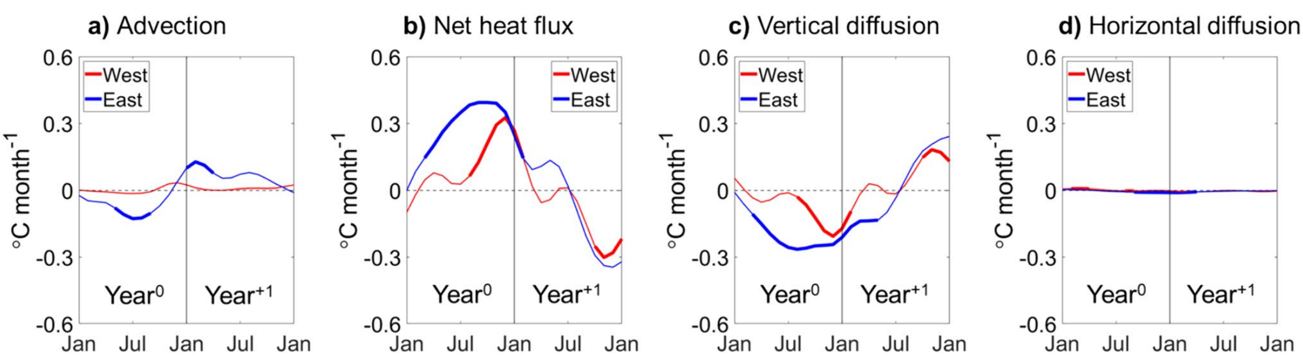

Fig. 7 Composite average of process-specific contribution on surface layer heat budget variations (in °C month^{-1}) in the Indonesian seas during El Niño years, including **a** advection; **b** surface net heat flux; **c** vertical diffusion at the base of surface layer (i.e., 20 m depth); and d) horizontal diffusion. Red and blue solid lines indicate the western and eastern Indonesian seas, respectively. Thicker solid line indicates period with statistically significant composite average at $p<0.1$ according to the two-tailed Student's *t*-test

although it further involves various factors for the La Niña to be fully developed (e.g., Mayer et al. 2018).

3.3 Surface layer heat budget variability decomposition

Process-specific contributions to the anomalous heat budget in the Indonesian seas during recent El Niño years are shown in Fig. 7, which consist of advection, surface net heat flux, vertical diffusion at the base of surface layer, and horizontal diffusion. A contrasting difference in the influence of ocean circulation (i.e., advection) on the overall heat budget variations can be observed where in the western Indonesian seas, the process did not contribute significantly. In the eastern part, advection resulted in a relatively pronounced anomalous cooling tendency during May^0–Sep^0 (–0.11 °C month^{-1}) and warming tendency anomalies from late Year^0 throughout Year^{+1}, including Nov^0–Mar^{+1} (+ 0.07 °C month^{-1}) and May^{+1}–Sep^{+1} (+ 0.07 °C month^{-1}).

Modulation in the surface net heat flux during El Niño years clearly has important contribution to the overall surface layer heat budget variations in the Indonesian seas, as denoted by the magnitude of the anomalous temperature tendency induced by the process in both selected areas. The anomalous temperature tendency due to the surface net heat flux in the western Indonesian seas even showed close resemblance with the overall temperature tendency anomalies in the area, highlighting its determining role in the overall heat budget variations. Of three El Niño phases used here, the strongest anomalous warming tendency due to the surface net heat flux in the western Indonesian seas occurred during Nov^0–Mar^{+1} (+ 0.21 °C month^{-1}) whereas in the eastern Indonesian seas, it occurred in May^0–Sep^0 (+ 0.34 °C month^{-1}).

Relaxation of the anomalous warming tendency due to the surface net heat flux in Year^{+1} further implies that the previously anomalous atmospheric condition was being restored. The temperature tendency anomalies due to the surface net heat flux in May^{+1}–Sep^{+1} was relatively weak in both selected areas (−0.05 °C month^{-1} and −0.01 °C month^{-1} for western and eastern Indonesian seas, respectively). At the end of Year^{+1}, the surface net heat flux induced an anomalous cooling tendency implying another swing in the overall atmospheric state following the demise of El Niño.

Variation in temperature tendency anomalies due to vertical diffusion at the base of the surface layer indicates the role of the process in counterbalancing the effect of the anomalous net heat flux at the surface (i.e., cooling and warming tendency anomalies in Year^0 and Year^{+1}, respectively). Anomalous heat accumulation in the surface layer in Year^0 due to the surface net heat flux strengthened the near-surface temperature vertical stratification, further led to an anomalous increase in the overall diffusive temperature flux into the water beneath the surface layer. Hence, an anomalous cooling tendency occurred as more heat was transmitted downward from the surface layer. The anomalous cooling tendency was strongest during Nov^0–Mar^{+1} (–0.14 °C month^{-1}) and May^0–Sep^0 (–0.24 °C month^{-1}) for the western and eastern Indonesian seas, respectively. The less-apparent temperature tendency anomalies during May^{+1}–Sep^{+1} (+ 0.02 °C month^{-1} and −0.02 °C month^{-1} for western and eastern Indonesian seas, respectively) from vertical diffusion commensurately balanced the weak modulation in the surface net heat flux. Conversely, anomalous heat loss in the surface layer in the end of Year^{+1} due to the surface net heat flux was coupled with warming tendency anomalies from the vertical diffusion at the base of the surface layer. The influence of horizontal diffusion on the heat budget variation contributed a small portion, which made it generally negligible; thus, it will be excluded from further discussion in this study.

3.4 Anomalous air–sea heat flux influence on heat budget variations

Figure 8 shows the components that comprise the Q_{Net} temperature tendency anomalies during El Niño years in the western and eastern Indonesian seas. From the temperature tendency magnitude perspective, the Q_{SW} and Q_{LH} anomalies exerted the strongest influence on the Q_{Net} temperature tendency anomalies. The anomalous warming tendency due

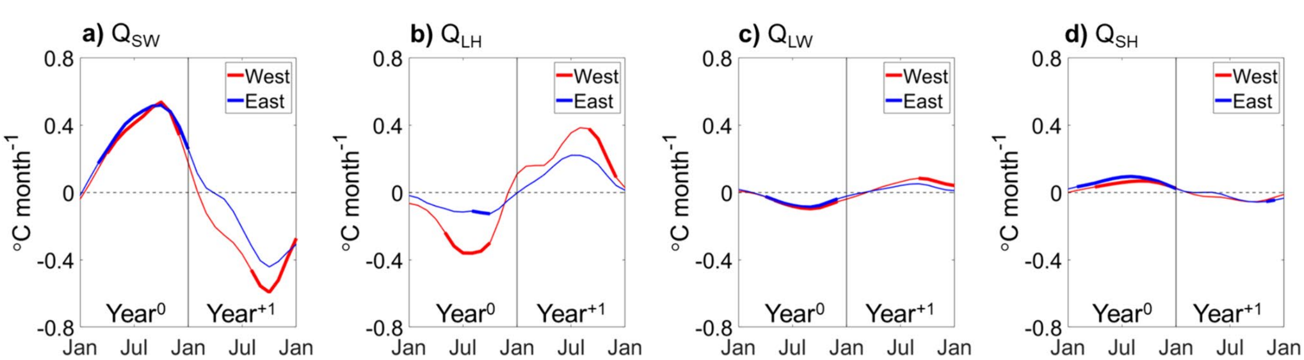

Fig. 8 Decomposition of anomalous surface layer temperature tendency (in °C month^{-1}) due to surface net heat flux during El Niño years, including **a** shortwave radiation 'Q_{SW}'; **b** latent heat flux 'Q_{LH}'; **c** net longwave radiation 'Q_{LW}'; and **d** sensible heat flux 'Q_{SH}' in western (red solid line) and eastern (blue solid line) Indonesian seas. Thicker solid line indicates period with statistically significant composite average at $p < 0.1$ according to the two-tailed Student's *t*-test

to Q_{SW} (i.e., stronger-than-usual incoming shortwave radiation) during El Niño years was strongest during May^0–Sep^0, averaging at + 0.41 °C month^{-1} and + 0.44 °C month^{-1} for the western and eastern Indonesian seas, respectively (Fig. 8a). Again, the warming tendency anomalies due to Q_{SW} were even higher during extreme events such as the 1997/98 El Niño when the May^0–Sep^0 anomalous warming tendency average was + 0.80 °C month^{-1} and + 0.51 °C month^{-1} for the western and eastern Indonesian seas, respectively (figure not shown).

As El Niño entered its mature phase in the transition from Year^0 to Year^{+1}, the anomalous warming tendency induced by Q_{SW} started to shift to an anomalous cooling tendency. This is indicated by the weaker warming tendency anomalies in Nov^0–Mar^{+1} of + 0.18 °C month^{-1} and + 0.25 °C month^{-1} for the western and eastern Indonesian seas, respectively. Further, the anomalous cooling tendency due to Q_{SW} anomalies, which imply weaker-than-usual incoming shortwave radiation, following the demise of El Niño during May^{+1}–Sep^{+1} were averaged at −0.39 °C month^{-1} and −0.22 °C month^{-1} for the western and eastern Indonesian seas, respectively. This overall result on the Q_{SW} temperature tendency anomalies highlight the robustness of anomalous atmospheric features across the Indonesian seas during El Niño as indicated by the earlier generation of reanalysis product used in Hendon (2003) which still in relatively coarse resolution.

The effect from Q_{LH} anomalies in the Indonesian seas during El Niño years (Fig. 8b) generally counteracted the anomalous Q_{SW} effect on the surface layer heat budget variations (i.e., anomalous cooling and warming tendency in Year^0 and Year^{+1}, respectively). During May^0–Sep^0, the stronger-than-usual Q_{LH} anomalies (i.e., enhanced evaporative heat loss from sea surface) resulted in anomalous cooling tendency of −0.32 °C month^{-1} and −0.11 °C month^{-1}, on average, for the western and eastern Indonesian seas, respectively. The Q_{LH} anomalies also experienced shifts in Nov^0–Mar^{+1} when they induced weak temperature tendency anomalies averaged at + 0.05 °C month^{-1} and −0.01 °C month^{-1} for the western and eastern Indonesian seas, respectively. The subtle Q_{LH} temperature tendency anomalies during Nov^0–Mar^{+1} makes the Q_{SW} become the only dominant component of Q_{Net} in driving the surface layer heat budget variations, particularly in western Indonesian seas where the Q_{LH} was previously strong enough to balance the Q_{SW}. The Q_{LH} continues to be anomalously weak (suppressed evaporative heat loss) in Year^{+1}, leading to warming tendency anomalies in both sections of Indonesian seas. Again, the anomalously weaker Q_{LH} in the western Indonesian seas were more notable than that in the eastern Indonesian seas. The average anomalous warming tendency during May^{+1}–Sep^{+1} in the western and eastern Indonesian seas due to Q_{LH} anomalies were + 0.32 °C month^{-1} and + 0.20 °C month^{-1}, on average, respectively.

The overall surface layer temperature tendency anomalies due to Q_{LW} (Fig. 8c) and Q_{SH} (Fig. 8d) were small in both selected areas in the Indonesian seas. Both the western and eastern Indonesian seas experienced anomalous cooling and warming tendency due to Q_{LW} anomalies during Year^0 and Year^{+1} of El Niño, respectively. Conversely, the Q_{SH} induced anomalous warming and cooling tendency during the same Year^0 and Year^{+1} of El Niño, respectively. The Q_{SH} and Q_{LW} temperature tendency anomalies in both western and eastern Indonesian seas were in similar magnitude. Thus, the completely opposite anomalous temperature tendency canceled each other out and did not result in pronounced variations in the surface layer heat budget throughout the El Niño years.

The examination of temperature tendency anomalies induced by each air–sea heat exchange components during El Niño years here signifies the various consequences related to the anomalous atmospheric condition on the Indonesian seas surface layer heat budget variations. On one hand, the almost-uniform anomalous increase in the Q_{SW} from May^0–Sep^0 to Nov^0–Mar^{+1} implies the large-scale reduction cloud cover across the Indonesian seas (Fig. 9a). This explains the similarity between the Q_{SW} temperature tendency anomalies in the western and eastern Indonesian seas especially during Year^0. On the other hand, the Q_{LH} which acted in moderating the anomalous heat changes due to Q_{SW} exhibited more spatially varying features within the Indonesian seas (Figs. 9b). The overall weaker Q_{LH} anomalies in the eastern Indonesian seas than that in the western Indonesian seas explains the peak of Q_{Net} warming tendency anomalies that occurred earlier in the eastern Indonesian seas and the close resemblance in the temperature tendency anomalies caused by the Q_{SW} and Q_{Net}.

Some studies have pointed out the role of anomalous wind circulation in modulating Q_{LH} anomalies, where higher wind speed leads to enhanced evaporative heat loss (stronger-than-usual Q_{LH}) into the atmosphere (Wang and McPhaden 2000; Hendon 2003; Kido et al. 2019). Hendon (2003) has provided a detailed explanation of anomalous atmospheric circulation in Indonesian seas during the development of El Niño and its possible consequences on the Q_{LH} anomalies. Specifically, anomalous easterly surface wind stress during May^0–Sep^0 enhanced the southeast monsoon circulation and ultimately enhance the Q_{LH} from the sea surface to the atmosphere. This is also evident from the simulation result especially in the western Indonesian seas that exhibit stronger wind stress anomalies than that in the eastern Indonesian seas (Fig. 9c). However, the same anomalous easterly surface wind stress in Nov^0–Mar^{+1} which weakened the northwest monsoon circulation (i.e., weaker-than-usual surface wind stress) did not result in

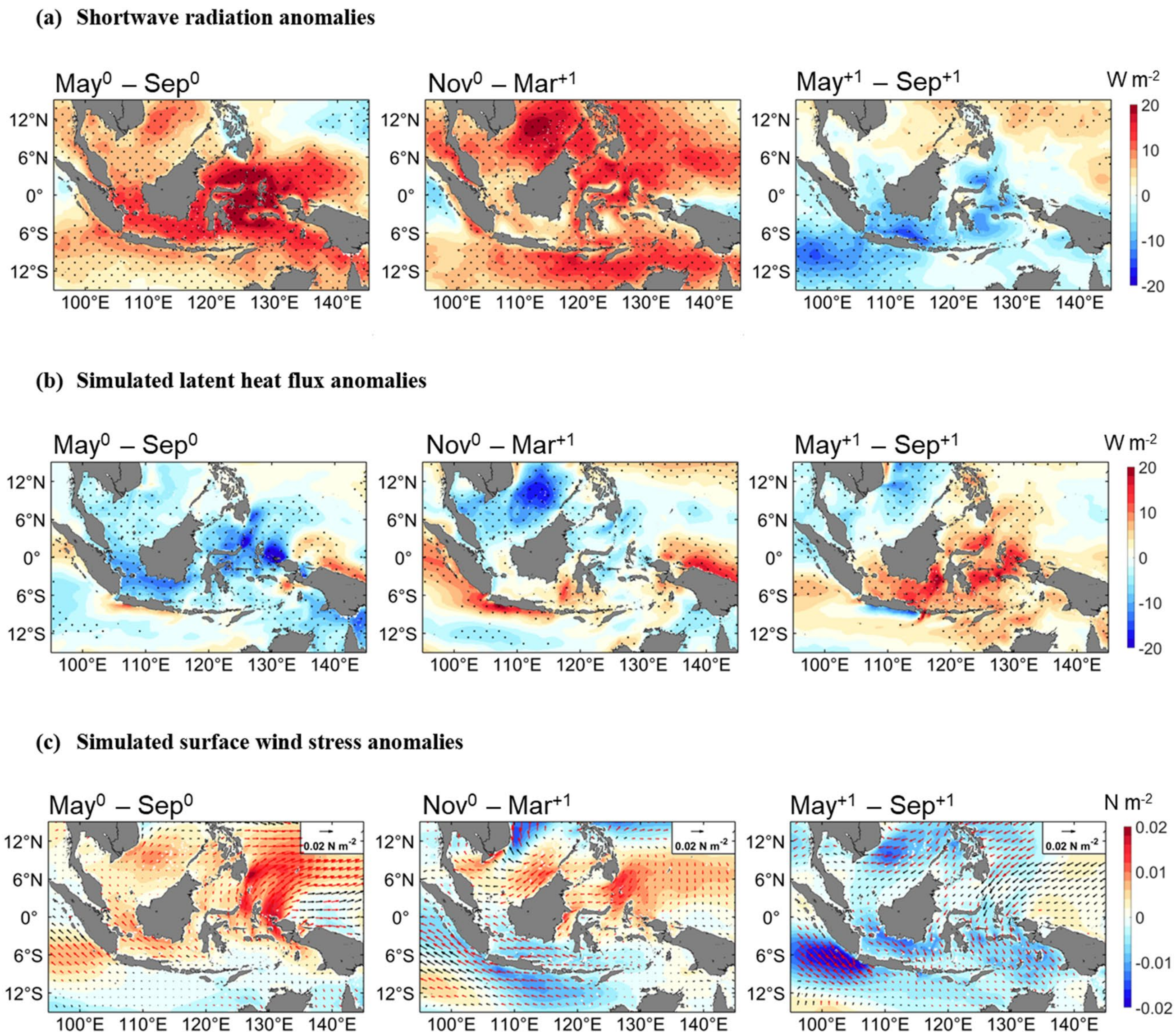

Fig. 9 Composite average of **a** incoming shortwave radiation Q_{SW} (Positive downward; in Watt m^{-2}); **b** latent heat flux Q_{LH} (Positive downward; in Watt m^{-2}); and **c** surface wind stress (vector arrows; in N m^{-2}) along with its magnitude (shading; in N m^{-2}) anomalies across the Indonesian seas during three stages of El Niño comprises the growth (May^0–Sep^0), mature (Nov^0–Mar^{+1}), and decay (May^{+1}–Sep^{+1}) phases. Areas with statistically significant composite average ($p < 0.01$) according to the two-tailed Student's *t*-test are marked by stippling and red-colored vector arrows

apparent Q_{LH} anomalies. We presume that because the Q_{LH} was previously in an anomalously stronger-than-usual state during May^0–Sep^0, the reduced surface wind stress during Nov^0–Mar^{+1} was more of a restoring force for the Q_{LH} toward neutral condition.

The notable anomalous Q_{LH} which later appeared during the May^{+1}–Sep^{+1} can be related to the persisting weaker-than-usual surface wind stress. Considering the high SST climatology in the area (De Deckker 2016), the emergence of warm SSTA following the El Niño mature phase likely introduced instability to the atmosphere and induced anomalous low-level convergence (Zhang and Mcphaden 1995; Hogikyan et al. 2022). This further maintained the weaker-than-usual surface wind stress which already developed from Nov^0–Mar^{+1} and ultimately led to anomalously smaller Q_{LH}. The Q_{LH} dependence on wind stress during El Niño years in both western and eastern Indonesian seas Q_{LH} were also evident from the simulation result (Supplementary Fig. 1). In addition to the influence from wind, the Q_{LH} is also function of air–sea humidity difference (Fairall et al. 1996). The anomalous atmospheric convergence, as implied from the anomalously low Q_{SW}, which occurred

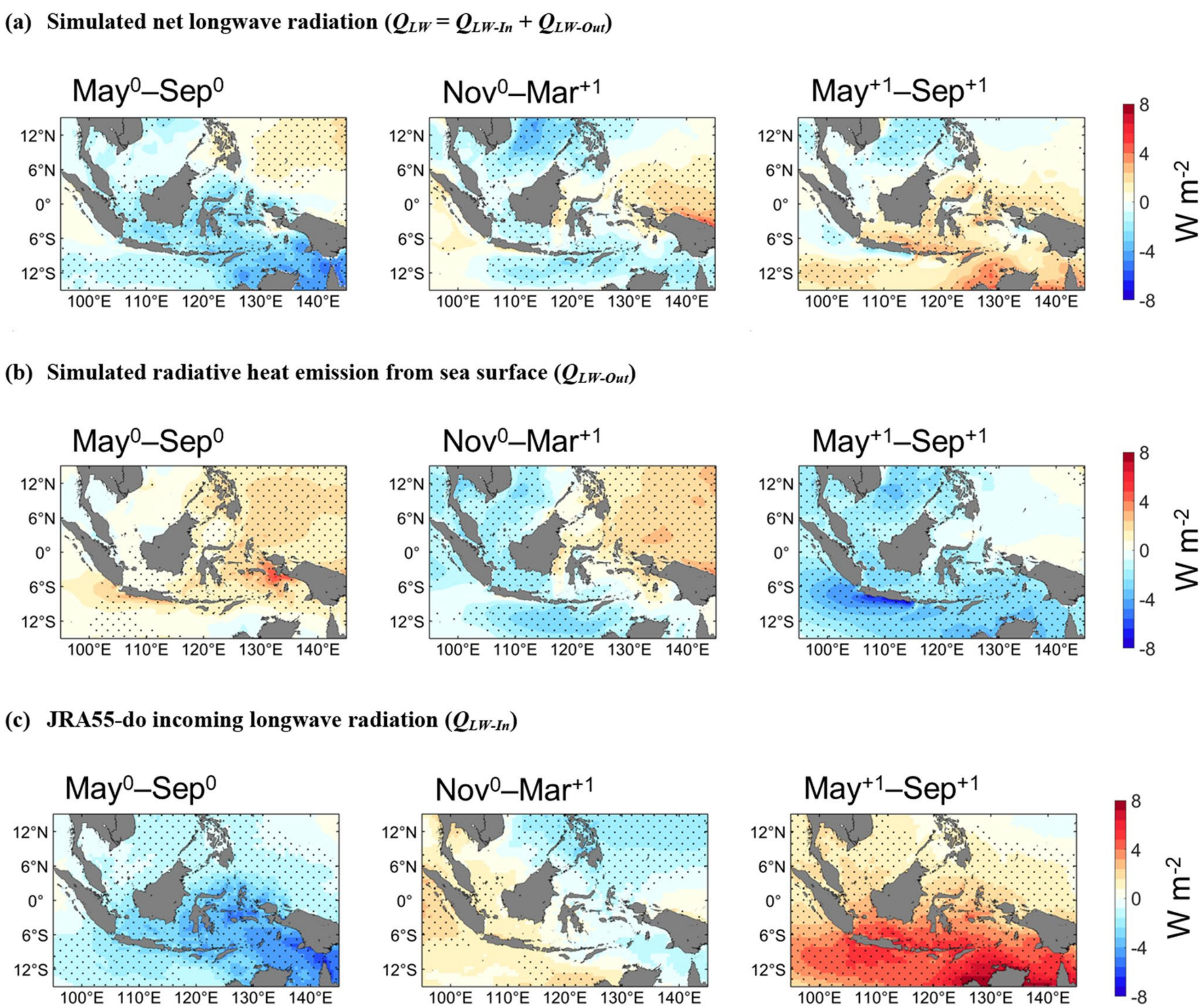

Fig. 10 Composite average of **a** simulated sea surface net anomalous longwave radiation (Q_{LW}; in W m^{-2}) calculated as a sum of **b** radiative heat emission from sea surface ($Q_{LW\text{-}out}$), which is a function of simulated sea surface temperature following the Stefan-Boltzmann Law for a non-black body assuming emissivity of 0.97; and **c** incoming longwave radiation anomaly ($Q_{LW\text{-}in}$) according to the JRA55-do atmospheric dataset used for this modeling study during three phase of El Niño events (growth May^0–Sep^0; mature Nov^0–Dec^{+1}; and decay May^{+1}–Sep^{+1}) over the study period (i.e., 1995–2019). Positive and negative anomalies indicate downward and upward direction, respectively. Areas with statistically significant composite average value ($p < 0.01$) according to the two-tailed Student's *t*-test are marked by stippling

in May^{+1}–Sep^{+1} could also affect the air–sea humidity difference through changes in the moisture flux convergence (Hagos et al. 2019; Alsepan and Minobe 2020) and affect the evaporation rate into the atmosphere.

The anomalous decrease in cloud cover which led to increase in the Q_{SW} during Year^0 of El Niño also associated with an increase in the outgoing longwave radiation (Giannini et al. 2007; Mayer et al. 2018). In line with this, the Q_{LW} cooling tendency anomalies in Year^0 indicated by the simulation result essentially implies an anomalous Q_{LW} that directed upward. The Q_{LW} warming tendency anomalies in Year^{+1} conversely, indicate an anomalous downward Q_{LW}. Figure 10 shows that most of the anomalous Q_{LW} across the interior part of Indonesian seas, including the selected western and eastern part for this study, was controlled by the incoming longwave radiation anomalies from the atmosphere ($Q_{LW\text{-}In}$) rather than the radiative heat emission from sea surface ($Q_{LW\text{-}Out}$).

Since the sea surface radiative heat emission is simply a function of SST, the reasons behind anomalous downward and upward $Q_{LW\text{-}Out}$ in Year^0 and Year^{+1}, respectively, are relatively straightforward (i.e., lower-than-usual SST in

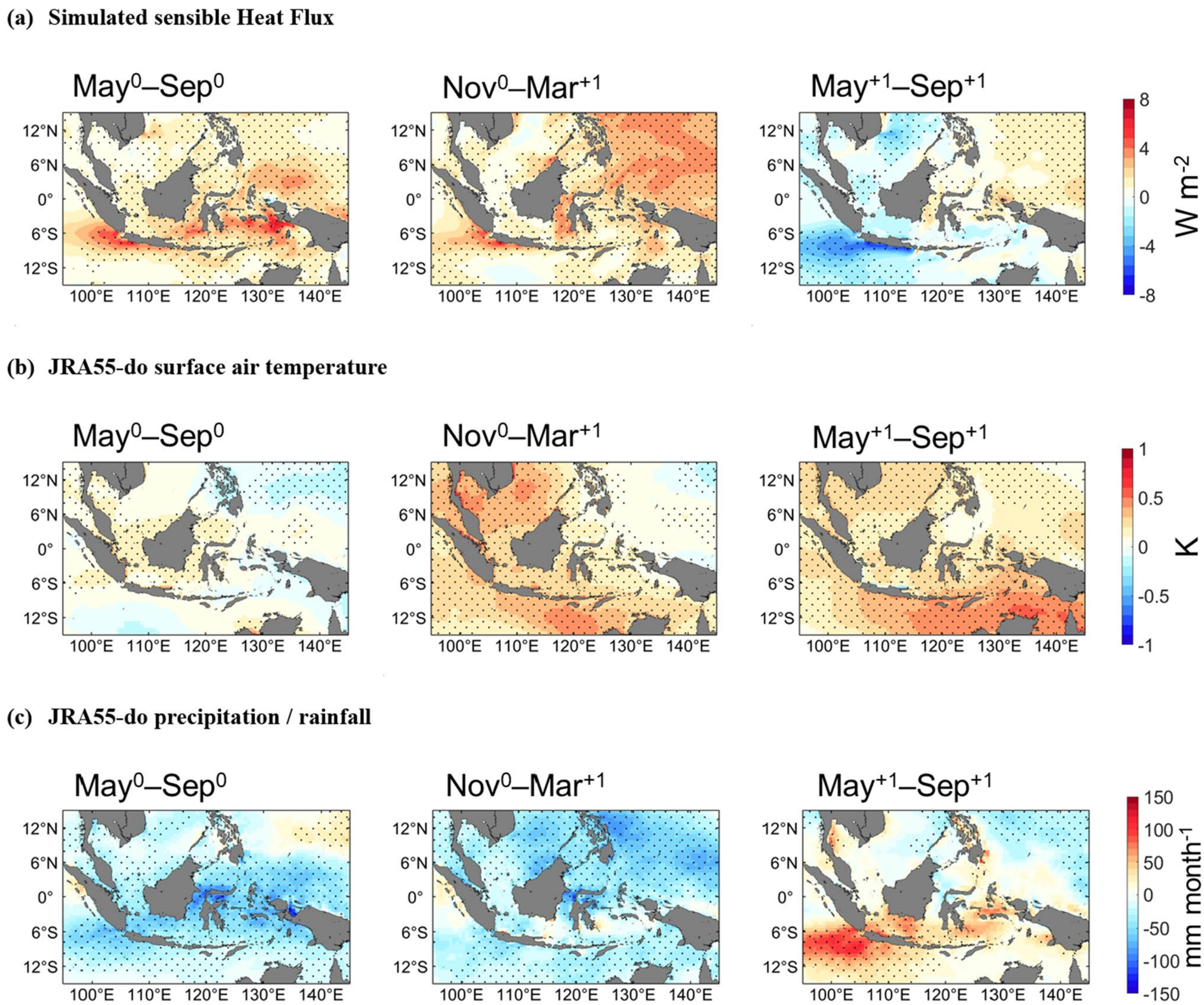

Fig. 11 Composite average of **a** simulated sea surface sensible heat flux anomalies (in W m^{-2}; positive downward); **b** surface air temperature (in K); and **c** precipitation (in mm month^{-1}) according to the JRA55-do atmospheric dataset used for this modeling study during three phase of El Niño years. Areas with statistically significant composite average value ($p<0.01$) according to the two-tailed Student's *t*-test are marked by stippling

Year^{0} will decrease the radiative heat emission and *vice versa* for higher-than-usual SST in Year^{+1}). Changes in the $Q_{LW\text{-}In}$ as indicated by the JRA55-do datasets on the other hand, involves several processes. Some studies based on observation and modeling have proposed the SST-cloud-Q_{LW} feedback mechanism in the tropics where higher-than-usual SST (e.g., Year^{+1} of El Niño) induces stronger convective activity, increases the cloudiness which in turn increases the $Q_{LW\text{-}In}$ owing to the enhanced heat trapping of the sea surface radiative heat emission (Wang and Enfield 2001; Sun et al. 2017). These cloud-enhanced heat trapping mechanism during anomalously warm SST (Year^{+1}) was also in agreement with the tropics-wide tropospheric warming (i.e., increase in the overall effective radiation temperature) during El Niño years (Angell 2000; Trenberth et al. 2002; Hogikyan et al. 2022). The opposite applies during anomalously lower-than-usual SST condition as well (i.e., Year^{0}).

The Q_{SH} warming tendency anomalies in Year^{0} indicates a downward heat flux anomalies (Fig. 11a) which can be explained by anomalous air–sea temperature gradient where the surface air temperature was anomalously warmer than that in the sea surface. Conversely, the cooling tendency anomalies due to Q_{SH} during Year^{+1} indicate a reversal in the overall air–sea temperature gradient anomalies. The cool and warm SSTA in Indonesian seas during Year^{0} and Year^{+1} obviously could trigger this anomalous air–sea temperature gradient even under the condition in which the surface air temperature did not exhibit strong anomalies. In fact however, the surface air temperature generally showed higher-than-usual value during El Niño (Lean and Rind 2008; Thirumalai et al. 2017; Jiang et al. 2024) which further contributes to the air–sea temperature gradient anomalies. Distribution of surface air temperature anomalies across the Indonesian seas from JRA55-do during El Niño years indeed show an almost persistent anomalous warm feature (Fig. 11b). This supports the idea of anomalous SST as main driver for the air–sea temperature gradient anomalies, given the relatively larger swing in the SSTA value as shown previously.

The precipitation also known for affecting the Q_{SH} although in relatively long time-scale (i.e., interannual timescale or longer), the contribution to the Q_{SH} low-frequency variabilities is likely to be minor as extreme precipitation, which typically appears in much shorter time-scales, will be required (Gosnell et al. 1995; Ramos et al. 2022). Normally, the precipitation induces cooling on the surface since the raindrop temperature, approximated by wet bulb temperature, tends to be lower than the sea surface temperature (Gosnell et al. 1995). Hence, both air–sea temperature gradient and precipitation anomalies during El Niño years are working in the same direction in driving the anomalous Q_{SH}. This is because the lower-than-usual and higher-than-usual precipitation (Fig. 11c) within the Indonesian seas led to precipitation-induced anomalous warming and cooling during Year^0 and Year^{+1}, respectively. Regression analysis on the Q_{SH} anomalies against both air–sea temperature gradient and precipitation anomalies confirm that the two processes, to a statistically significant extent, influenced the overall Q_{SH} variances during El Niño years (Supplementary Fig. 2).

3.5 The role of ocean circulation in the eastern Indonesian seas

Examination of the temperature tendency anomalies due to advection was focused on the eastern Indonesian seas, as the process exhibited a pronounced influence on the overall heat budget variations in the area. The advection of anomalous

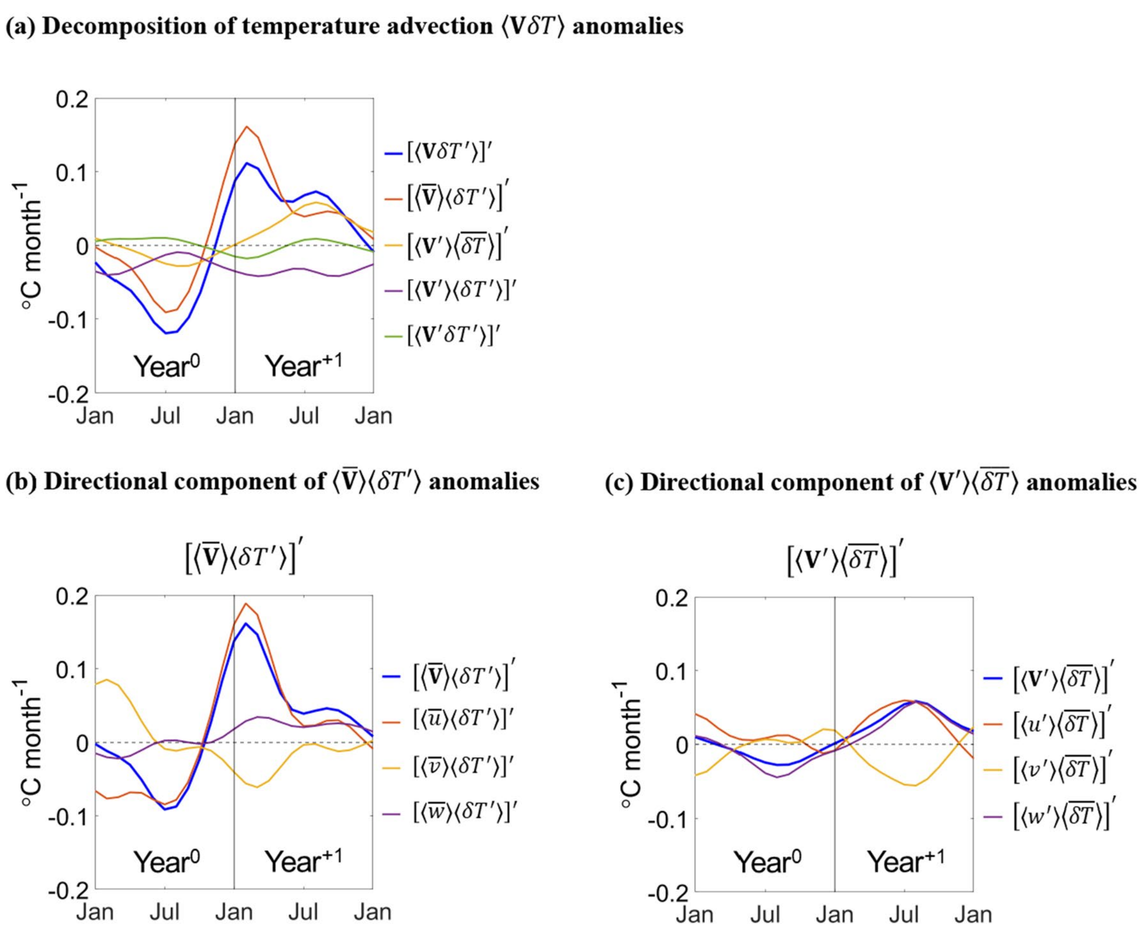

Fig. 12 Temperature tendency anomalies (in °C month^{-1}) in the eastern Indonesian seas during El Niño years due to **a** advection process; advection of **b** anomalous temperature by mean circulation; and advection of **c** mean temperature by anomalous circulation along with its directional component

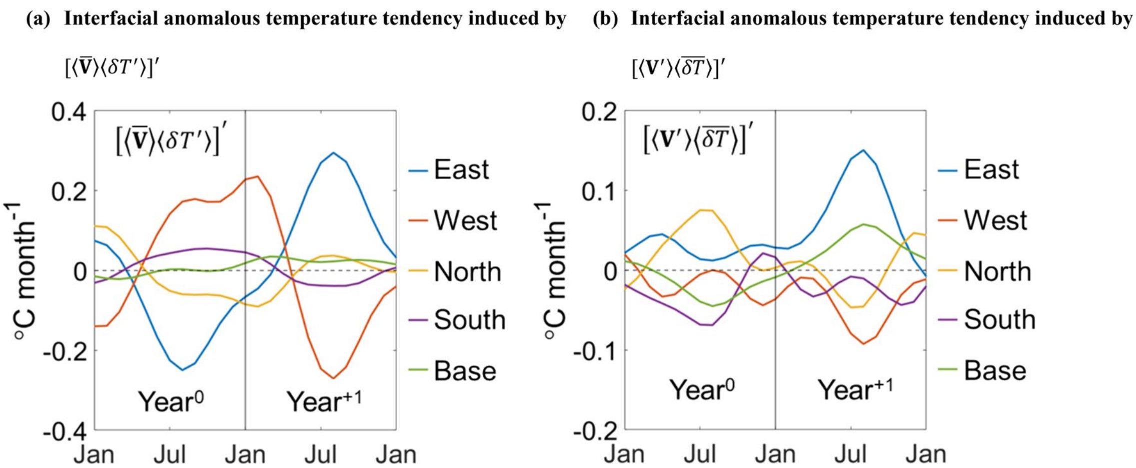

Fig. 13 Anomalous surface layer temperature tendency (in °C month^{-1}) at each interface of the eastern Indonesian seas due to **a** advection of anomalous temperature by mean circulation $\left[\left\langle\overline{\mathbf{V}}\right\rangle\langle\delta T'\rangle\right]'$ and **b** advection of mean temperature by anomalous circulation $\left[\langle\mathbf{V}'\rangle\left\langle\overline{\delta T}\right\rangle\right]'$. Note the different scale in the y-axis between the two figures

warmer/cooler water $\left[\left\langle\overline{\mathbf{V}}\right\rangle\langle\delta T'\rangle\right]'$ closely resembled the overall temperature tendency anomalies due to advection during El Niño years (Fig. 12a). For this reason, $\left[\left\langle\overline{\mathbf{V}}\right\rangle\langle\delta T'\rangle\right]'$ can be regarded as the dominant component driving heat budget variations in the context of temperature advection anomalies. Anomalous cooling and warming tendencies during May^0–Sep^0 and May^{+1}–Sep^{+1} due to $\left[\left\langle\overline{\mathbf{V}}\right\rangle\langle\delta T'\rangle\right]'$ were notably enhanced by temperature advection due to anomalous circulation $\left[\langle\mathbf{V}'\rangle\left\langle\overline{\delta T}\right\rangle\right]'$ as shown in Fig. 12b, c. Whereas, the other temperature advection anomalies components (i.e., $\left[\langle\mathbf{V}'\rangle\langle\delta T'\rangle\right]'$ and $\left[\langle\mathbf{V}'\delta T'\rangle\right]'$ did not significantly contribute to the overall heat budget variations in the area. Further decomposition of $\left[\left\langle\overline{\mathbf{V}}\right\rangle\langle\delta T'\rangle\right]'$ shows that the advection of anomalously cooler and warmer water into the eastern Indonesian seas during El Niño years mostly related to the transport of anomalous heat in the zonal direction $\left(\left[\langle\overline{u}\rangle\langle\delta T'\rangle\right]'\right)$.

Circulation features within the Indonesian seas, including the eastern Indonesian seas, can be characterized by an alternating eastward–westward surface current that closely aligns with the seasonal monsoon circulation (Kartadikaria et al. 2012). This was further reflected in the interfacial heat transport anomalies of the eastern Indonesian seas, where the east–west interface showed the strongest influence on the eastern Indonesian seas surface layer heat budget variations during El Niño years (Fig. 13a). The westward current during the southeast monsoon season, which coincided with the May^0–Sep^0 / May^{+1}–Sep^{+1} period, brought anomalously

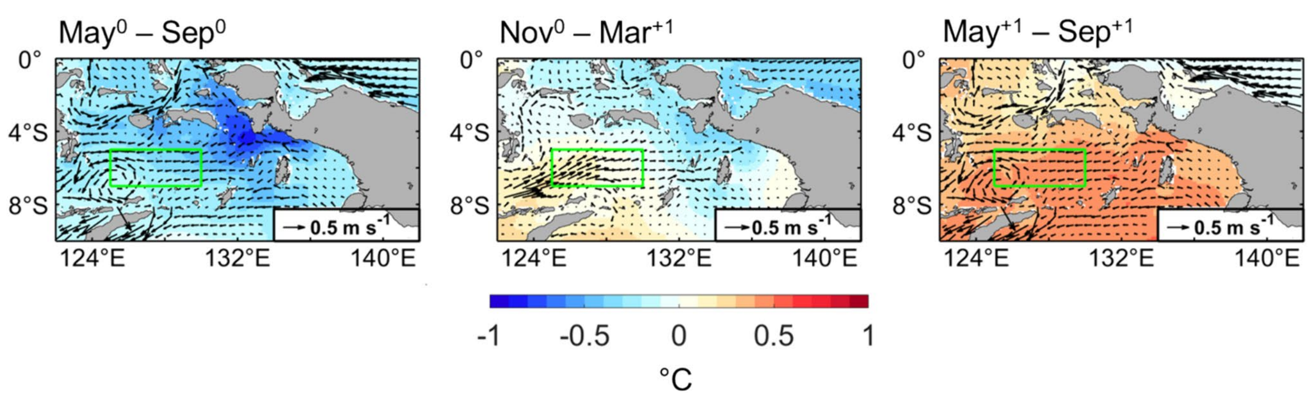

Fig. 14 Composite average of temperature anomalies (shaded color, in °C) overlaid with the seasonal ocean circulation features (vector arrows, in m s^{-1}) around the eastern Indonesian seas during three phases of El Niño; May^0–Sep^0 (left panel), Nov^0–Mar^{+1} (middle panel), and May^{+1}–Sep^{+1} (right panel). Green box indicates the area of interest where heat budget analysis was performed

cool (cooling tendency anomalies at the east interface) and warm (warming tendency anomalies at the east interface) water during the growth and decay phases of El Niño, respectively. On the other hand, the eastward surface current during the El Niño mature phase of Nov^{0}–Mar^{+1} (i.e., northwest monsoon season) brought anomalous warm water originating from the area around the southern part of the Makassar Strait into the eastern Indonesian seas (warming tendency anomalies at the west interface).

The amplification of cooling and warming tendency anomalies during May^{0}–Sep^{0} and May^{+1}–Sep^{+1} owing to anomalous circulation mainly came in the form of anomalous entrainment ($w' > 0$) and detrainment ($w' < 0$) of cool water ($\overline{\delta T} < 0$) beneath the surface layer (Fig. 13b). Anomalous entrainment in Year^{0} and detrainment in Year^{+1}, which accompanied with negative and positive SSHA, respectively, imply that anomalous volume divergence and convergence occurred in the area. This is consistent with the altimetry-based estimation in the area done by Gordon and Susanto (2001) albeit the relatively short period of coverage (1993–1999). This result also suggests that the robust SSHA during El Niño years, along with associated anomalous circulation features which led to the divergence anomalies, does not necessarily imply a strong influence on the SSTA development in the area.

The spatial distribution of the SSTA further indicate the varying contribution of anomalous temperature and mean ocean circulation in driving surface layer heat budget anomalies during different phases of El Niño (Fig. 14). In particular, strong cooling and warming tendency anomalies during May^{0}–Sep^{0} and May^{+1}–Sep^{+1} were driven by strong anomalous cool and warm water entering the eastern Indonesian seas from the eastern part of the Banda Sea. In contrast, the warming tendency anomaly during Nov^{0}–Mar^{+1} was driven by a strong eastward current around the western interface. The role of ocean circulation as a deciding factor during Nov^{0}–Mar^{+1} was based on the overall SSTA during the period that was notably milder than that in the May^{0}–Sep^{0} and May^{+1}–Sep^{+1} yet the west interface exhibited strong warming tendency anomalies.

Examination of the influence of ocean circulation in driving heat budget variations in eastern Indonesian conducted here partly confirms the hypothesis proposed by Iskandar et al. (2020) about the advection of anomalous temperature into the Indonesian seas during El Niño. Additional details on the anomalous temperature advection were revealed through the heat budget analysis, including the eastward spread of anomalous warm water from the southern Makassar Strait during Nov^{0}–Mar^{+1}. Similar mechanism driving warm SSTA in the western Indonesian seas (i.e., surface net heat flux-induced warming tendency anomalies) was responsible for inducing the warm SSTA in the southern Makassar Strait which further transported to the eastern Indonesian seas. This was based on the distribution of Q_{SW} and Q_{LH} anomalies during three El Niño phases in the Indonesian seas which was shown previously.

On the other hand, the cooling and warming tendency anomalies in the eastern Indonesian seas were primarily sourced from anomalous surface water around the northern Arafura Sea during May^{0}–Sep^{0} and May^{+1}–Sep^{+1}, respectively. The cool SSTA from the northern Arafura Sea was likely part of upwelling system in the area (Basit et al. 2022) which enhanced in response to stronger southeasterly wind stress during May^{0}–Sep^{0}. Conversely, the upwelling also suppressed during May^{+1}–Sep^{+1} given the weaker surface wind stress which led to warm SSTA which further spread eastward through the seasonal ocean circulation. Results from examination here suggests that the influence of cooler-than-usual SST from the western Pacific, which usually appears during El Niño, on Indonesian seas was likely less robust than previously presumed. There might be a fraction of western pacific surface water that transported during May^{0}–Sep^{0} and May^{+1}–Sep^{+1} into eastern Indonesian seas although it requires further analysis involving other methods such as particle tracking experiment (e.g., Kartadikaria et al. 2012; Iskandar et al. 2023).

3.6 Idealized case of the linkage between El Niño-like heat budget variation and corresponding temperature anomalies pattern

Compared to the emerged warm SSTA, which lasted for almost a year following the mature phase of El Niño, the anomalous low-frequency warming tendency within the Indonesian seas suggests a heat budget perturbation that occurred at a shorter time-scale. It has been strongly suggested that perturbation at a relatively short time-scale could lead to low-frequency variability (Meehl et al. 2001, 2021). The anomalous warming tendency/heat accumulation that occurred during the El Niño peak of approximately 2–4 months was sufficient to induce a shift in the mean state of heat content within the surface layer. The lack of commensurate-and-immediate cooling tendency anomalies in the subsequent year after El Niño further extended the higher-than-usual mean state, which ultimately realized as the anomalous warm SST. Only when anomalous cooling tendency started to appear in Year^{+1} did the SST anomalies begin to be relaxed as the previously perturbed heat content mean state was restored.

A simple one-dimensional heat budget variation model with idealized perturbation was employed and is shown in Fig. 15 to prove our presumption. The idealized model was set with a hypothetical temperature tendency which correspond to normal condition (i.e., no anomalies) but closely follows the heat budget cycle periodicity in Indonesian seas

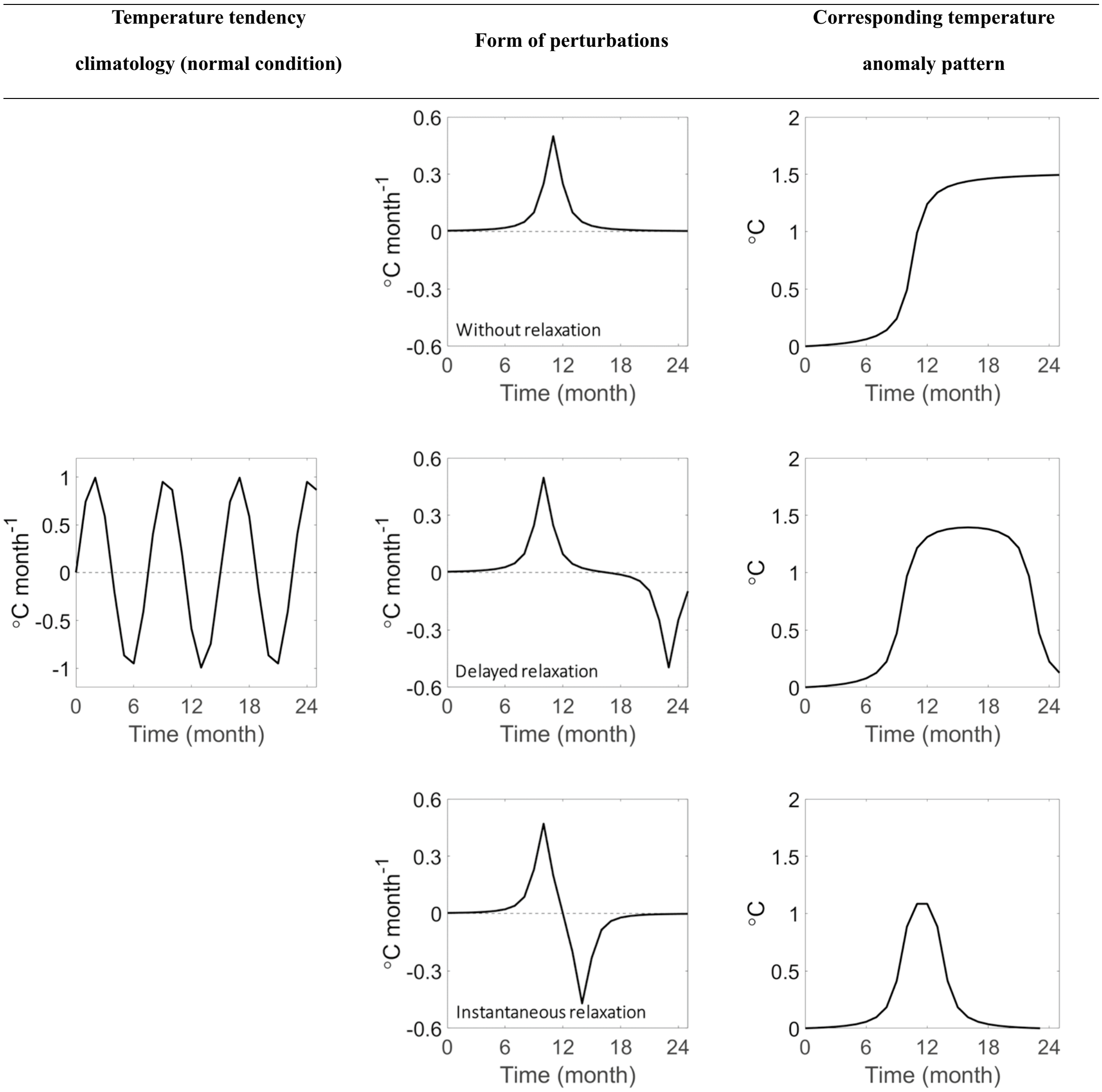

Fig. 15 Analysis on the temperature anomalies response (in °C) and its sensitivity toward idealized El Niño-like perturbation in the heat budget (in °C month^{-1}) and different types of cooling tendency anomalies

found in Amri et al. (2024). The temperature tendency further perturbed by several form of anomalous temperature tendency, with one perturbation form closely resembled the El Niño-like warming tendency anomalies and further followed by cooling tendency anomalies (i.e., delayed relaxation), which closely mimic the anomalous temperature tendency in the selected two areas in Indonesian seas during the El Niño years. The delayed relaxation-type perturbation resulted in the persistent warm SSTA pattern that later followed by relaxation which again, captured the overall SSTA pattern following the mature phase of El Niño exhibited by both selected areas in the Indonesian seas. Therefore, the emerged warm SSTA in Year^{+1} in the Indonesian seas was the result of heat budget perturbation that occurred in Nov^{0}–Mar^{+1}. The slightly warmer SSTA in the eastern Indonesian seas during May^{+1}–Sep^{+1} further can be attributed further to the longer warming tendency anomalies in the area, where the advection process was responsible for extending the heat budget perturbation.

Similarly, the cool SSTA in the eastern Indonesian seas during May^{0}–Sep^{0} can be attributed to the cooling tendency anomalies started even before Year^{0} (Supplementary Fig. 3). The cooling tendency anomalies were not as strong as in the end of Year^{+1} but long enough, lasting up to August of Year^{0}, that it can induced notable changes in the temperature. This was in contrast with the western Indonesian seas where the early Year^{0} cooling tendency anomalies, which also commenced before Year^{0}, occurred for a shorter period that lasted only until February of Year^{0}. Hence, the less-apparent cool SSTA than that in the eastern Indonesian seas during May^0–Sep^0. Note that longer period of cooling/warming tendency anomalies also could lead to stronger cool/warm SSTA considering the accumulation that occurred throughout the anomalous period.

4 Concluding remarks

The underlying mechanism of emerging sea surface temperature anomalies in the Indonesian seas during El Niño events over the 1995–2019 period was investigated for the first time through a complete surface layer heat budget analysis. We used a similar ocean model as in Kido et al. (2019) and Murata et al. (2020) that could compute the heat budget components simultaneously with the actual ocean circulation model run (i.e., online), ensuring budget closure throughout the model integration. The closure of the heat budget becomes important for this type of study to prevent possible misinterpretation caused by residual signals that usually appear in an offline heat budget analysis (e.g., Iskandar et al. 2020; Ismail et al. 2023). A detailed understanding about natural phenomenon, which is known to have severe consequences on people livelihood will help the related stakeholders to respond accordingly. The complete heat budget analysis framework employed here is also relevant for complementing studies about phenomenon in shorter time-scales such as marine heatwave events (e.g., Beliyana et al. 2023).

Modulation in the surface layer heat budget in the western Indonesian seas was predominantly controlled by variations in the air–sea heat exchange, specifically the shortwave radiation and latent heat flux, with other processes (i.e., ocean circulation and mixing) contributing to minor effects on overall heat budget variations. In contrast, the eastern part of the Indonesian seas exhibited a pronounced influence from ocean circulation in addition to the surface net heat flux. The effect of ocean circulation was even comparable to the influence of sea surface net heat flux and vertical diffusion combined, explaining the subtle net cooling tendency anomalies in the area during the El Niño growth phase despite the strong warming tendency anomalies induced by the surface net heat flux. Ocean circulation in the eastern part of the Indonesian seas was also responsible for prolonging anomalous warming tendency (heat accumulation) in the area following the mature phase of El Niño. The anomalous heat accumulation, peaked during the mature phase of El Niño, ultimately led to the emergence of warm SSTA in the Indonesian seas as early as in the Boreal Autumn of Year^0 and lasted for almost a year until Year^{+1} even after the El Niño itself already decayed. The absence of anomalous cooling tendency, except at the late of Year^{+1}, explains the persisting warm SSTA in the areas selected for this study.

In some El Niño years which concurrent with extreme pIOD, such as the 1997 pIOD (Liu et al. 2017) which overlapped the 1997/98 El Niño, a stronger warming tendency anomaly was suggested by the model particularly in the western Indonesian seas. Similar to the El Niño, the pIOD is also associated with decrease in the cloud cover around the eastern Indian Ocean, where the western Indonesian seas situated, which could lead to increased incoming solar radiation (Ng et al. 2014). The shortwave radiation anomalies from the atmospheric forcing dataset used in this study, as well as the overall simulated sea surface net heat flux, showed positive correlation with the IOD from Boreal Summer to Boreal Winter (Supplementary Figs. 4, 5). This is also in agreement with the pIOD-focused heat budget study by Delman et al. (2018) where the sea surface net heat flux, driven by shortwave radiation, showed strong warming tendency anomaly on the south of Java mixed layer.

Completely isolating the IOD effect on ENSO (or vice versa) along with its influence on the surface layer heat budget variations in the Indonesian seas was not the intent of this study. It is still very challenging to completely extract a particular variability from the datasets that resulted from various climatic/weather signals interaction (Li et al. 2019). A more sophisticated modeling studies experiment through rigorous modification in the forcing datasets (e.g., Maher et al. 2018; Kido et al. 2019) or utilization of a fully coupled climate model with synthetic scenario (e.g., Kosaka and Xie 2013) offers a more promising approach to address this issue and warrants further studies in the future. Regardless, the study conducted here may provide valuable insight on the detailed mechanism behind the emerged SSTA during recent El Niño years quantitatively and contribute to the advancement of our understanding about air–sea interaction in the Indonesian seas.

Supplementary Information The online version contains supplementary material available at https://doi.org/10.1007/s10872-024-00728-6.

Acknowledgements We are grateful to the two anonymous reviewers for their time in providing constructive comments that greatly improved this manuscript. The first author was a scholarship recipient offered for foreign students from the Ministry of Education, Culture, Science, and Technology (MEXT) Japan from 2017 to 2022.

Data availability The authors declare that the data used in this study are publicly available. The utilized source code of COAWST can be accessed at https://github.com/NakamuraTakashi. The monthly average ECMWF-ORAS5 ocean reanalysis product for model initialization and boundary conditions is available from https://cds.climate.copernicus.eu/cdsapp#!/dataset/reanalysis-oras5?tab=overview. Bathymetry data of GEBCO2022 (configured at 15-arc second grid) is available at https://www.gebco.net/. Atmospheric dataset of JRA55-do for model forcing is available at https://climate.mri-jma.go.jp/pub/ocean/JRA55-do/jra55do_latest.html for 2020 up to recent period and https://esgf-node.llnl.gov/search/input4mips/ for the period prior to 2020, respectively. Global tide model from Oregon State University (i.e., TPXO) is available at https://www.tpxo.net/global/. Satellite-derived J-OFURO3 dataset is available through the APDRC data repository at http://apdrc.soest.hawaii.edu/datadoc/jofuro3.php. World Ocean Atlas 2018 for the sea surface salinity climatological data is available at https://www.ncei.

noaa.gov/access/world-ocean-atlas-2018/. NINO3.4 and DMI time-series over the 1995–2019 period are available at https://psl.noaa.gov/gcos_wgsp/Timeseries/. MATLAB scripts for processing the model input and output are available upon reasonable request.

References

Ahn J, Lee Y (2022) Spatial gap-filling of GK2A daily sea surface temperature (SST) around the Korean peninsula Using meteorological data and regression residual kriging (RRK). Remote Sensing 14:5265. https://doi.org/10.3390/rs14205265

Alexander MA, Bladé I, Newman M et al (2002) The atmospheric bridge: the influence of ENSO teleconnections on air-sea interaction over the global oceans. J Clim 15:2205–2231. https://doi.org/10.1175/1520-0442(2002)015%3c2205:TABTIO%3e2.0.CO;2

Alsepan G, Minobe S (2020) Relations between interannual variability of regional-scale indonesian precipitation and large-scale climate modes during 1960–2007. J Clim 33:5271–5291. https://doi.org/10.1175/JCLI-D-19-0811.1

Amri F, Eladawy A, Nakamura T (2024) Sea surface temperature budget in Indonesian seas: the role of vertical turbulent flux and its east–west variations. IOP Conf Ser Earth Environ Sci 1350:012005. https://doi.org/10.1088/1755-1315/1350/1/012005

Angell JK (2000) Tropospheric temperature variations adjusted for El Niño, 1958–1998. J Geophys Res 105:11841–11849. https://doi.org/10.1029/2000JD900044

Basit A, Mayer B, Pohlmann T (2022) The effects of the Indonesian throughflow, river, and tide on physical and hydrodynamic conditions during the wind- driven upwelling period north of the Aru islands. JST 30:1689–1716

Beliyana E, Ningsih NS, Gunawan SR, Tarya A (2023) Characteristics of marine heatwaves in the indonesian waters during the PDO, ENSO, and IOD phases and their relationships to net surface heat flux. Atmosphere 14:1035. https://doi.org/10.3390/atmos14061035

Chapman DC (1985) Numerical treatment of cross-shelf open boundaries in a Barotropic coastal ocean model. J Phys Oceanogr 15:1060–1075. https://doi.org/10.1175/1520-0485(1985)015%3c1060:NTOCSO%3e2.0.CO;2

Chen B, Xie L, Zheng Q et al (2020) Seasonal variability of mesoscale eddies in the Banda sea inferred from altimeter data. Acta Oceanol Sin 39:11–20. https://doi.org/10.1007/s13131-020-1665-2

Cheng L (2024) Sensitivity of ocean heat content to various instrumental platforms in global ocean observing systems. Ocean-Land-Atmos Res 3:0037

De Deckker P (2016) The Indo-Pacific warm pool: critical to world oceanography and world climate. Geosci Lett. https://doi.org/10.1186/s40562-016-0054-3

Delman AS, Sprintall J, McClean JL, Talley LD (2016) Anomalous Java cooling at the initiation of positive Indian ocean dipole events. J Geophys Res Oceans. https://doi.org/10.1002/2016JC011635

Delman AS, McClean JL, Sprintall J et al (2018) Process-specific contributions to anomalous java mixed layer cooling during positive IOD events. J Geophys Res Oceans 123:4153–4176. https://doi.org/10.1029/2017JC013749

Egbert GD, Erofeeva SY (2002) Efficient inverse modeling of barotropic ocean tides. J Atmos Oceanic Tech 19:183–204. https://doi.org/10.1175/1520-0426(2002)019%3c0183:EIMOBO%3e2.0.CO;2

Fairall CW, Bradley EF, Rogers DP et al (1996) Bulk parameterization of air-sea fluxes for tropical ocean-global atmosphere coupled-ocean atmosphere response experiment. J Geophys Res 101:3747–3764. https://doi.org/10.1029/95JC03205

Fairall CW, Bradley EF, Hare JE et al (2003) Bulk parameterization of air-sea fluxes: updates and verification for the COARE algorithm. J Clim 16:571–591. https://doi.org/10.1175/1520-0442(2003)016%3c0571:BPOASF%3e2.0.CO;2

Feng M, Zhang Y, Hendon HH et al (2021) Niño 4 west (Niño-4W) sea surface temperature variability. JGR Oceans. https://doi.org/10.1029/2021JC017591

Flather RA (1976) A tidal model of the north-west European continental shelf. Mem Soc Roy Sci Liege. 10:141–164

Giannini A, Robertson AW, Qian J-H (2007) A role for tropical tropospheric temperature adjustment to El Niño-Southern Oscillation in the seasonality of monsoonal Indonesia precipitation predictability. J Geophys Res. https://doi.org/10.1029/2007JD008519

Gordon AL (2005) Oceanography of the Indonesian seas and their throughflow. Oceanography 18:15–27. https://doi.org/10.5670/oceanog.2005.01

Gordon AL, Susanto RD, Ffield A (1999) Throughflow within Makassar strait. Geophys Res Lett 26:3325–3328. https://doi.org/10.1029/1999GL002340

Gordon AL, Susanto RD (2001) Banda sea surface-layer divergence. Ocean Dyn 52:2–10. https://doi.org/10.1007/s10236-001-8172-6

Gordon AL, Napitu A, Huber BA et al (2019) Makassar strait throughflow seasonal and interannual variability: an overview. J Geophys Res Oceans 124:3724–3736. https://doi.org/10.1029/2018JC014502

Gosnell R, Fairall CW, Webster PJ (1995) The sensible heat of rainfall in the tropical ocean. J Geophys Res 100:18437–18442. https://doi.org/10.1029/95JC01833

Griffies SM, Hallberg RW (2000) Biharmonic friction with a Smagorinsky-like viscosity for use in large-scale eddy-permitting ocean models. Mon Weather Rev 128:2935–2946. https://doi.org/10.1175/1520-0493(2000)128%3c2935:bfwasl%3e2.0.co;2

Griffies SM, Danabasoglu G, Durack PJ et al (2016) OMIP contribution to CMIP6: experimental and diagnostic protocol for the physical component of the ocean model intercomparison project. Geosci Model Dev 9:3231–3296. https://doi.org/10.5194/gmd-9-3231-2016

Hagos S, Zhang C, Leung LR et al (2019) A zonal migration of monsoon moisture flux convergence and the strength of Madden-Julian oscillation events. Geophys Res Lett 46:8554–8562. https://doi.org/10.1029/2019GL083468

Halkides D, Lee T, Kida S (2011) Mechanisms controlling the seasonal mixed-layer temperature and salinity of the Indonesian seas. Ocean Dyn 61:481–495. https://doi.org/10.1007/s10236-010-0374-3

Hasson AEA, Delcroix T, Dussin R (2013) An assessment of the mixed layer salinity budget in the tropical Pacific ocean. Observations and modelling (1990–2009). Ocean Dyn 63:179–194. https://doi.org/10.1007/s10236-013-0596-2

Hendon HH (2003) Indonesian rainfall variability: impacts of ENSO and local air-sea interaction. J Climate 16:1775–1790. https://doi.org/10.1175/1520-0442(2003)016%3c1775:IRVIOE%3e2.0.CO;2

Hogikyan A, Resplandy L, Fueglistaler S (2022) Cause of the intense tropics-wide tropospheric warming in response to El Niño. J Clim 35:2933–2944. https://doi.org/10.1175/JCLI-D-21-0728.1

Horii T, Ueki I, Ando K (2018) Coastal upwelling events along the southern coast of Java during the 2008 positive Indian ocean dipole. J Oceanogr 74:499–508. https://doi.org/10.1007/s10872-018-0475-z

Huang B, Liu C, Banzon V et al (2021) Improvements of the daily optimum interpolation sea surface temperature (DOISST) version 2.1. J Clim 34:2923–2939. https://doi.org/10.1175/JCLI-D-20-0166.1

Iskandar I, Mardiansyah W, Lestari DO, Masumoto Y (2020) What did determine the warming trend in the Indonesian sea? Prog Earth Planet Sci. https://doi.org/10.1186/s40645-020-00334-2

Iskandar MR, Jia Y, Sasaki H et al (2023) Effects of high-frequency flow variability on the pathways of the Indonesian throughflow. JGR Oceans. https://doi.org/10.1029/2022JC019610

Ismail MFA, Karstensen J, Ribbe J et al (2023) Seasonal mixed layer temperature and salt balances in the Banda Sea observed by an Argo float. Geosci Lett 10:10. https://doi.org/10.1186/s40562-023-00266-x

Jiang N, Zhu C, Hu Z-Z et al (2024) Enhanced risk of record-breaking regional temperatures during the 2023–24 El Niño. Sci Rep 14:2521. https://doi.org/10.1038/s41598-024-52846-2

Kämpf J (2016) On the majestic seasonal upwelling system of the Arafura Sea. JGR Oceans 121:1218–1228. https://doi.org/10.1002/2015JC011197

Kartadikaria AR, Miyazawa Y, Nadaoka K, Watanabe A (2012) Existence of eddies at crossroad of the Indonesian seas. Ocean Dyn 62:31–44. https://doi.org/10.1007/s10236-011-0489-1

Kida S, Wijffels S (2012) The impact of the Indonesian throughflow and tidal mixing on the summertime sea surface temperature in the western Indonesian Seas. J Geophys Res Oceans 117:1–14. https://doi.org/10.1029/2012JC008162

Kido S, Tozuka T, Han W (2019) Anatomy of salinity anomalies associated with the positive Indian ocean dipole. JGR Oceans 124:8116–8139. https://doi.org/10.1029/2019JC015163

Kosaka Y, Xie SP (2013) Recent global-warming hiatus tied to equatorial Pacific surface cooling. Nature 501:403–407. https://doi.org/10.1038/nature12534

Lean JL, Rind DH (2008) How natural and anthropogenic influences alter global and regional surface temperatures: 1889 to 2006. Geophys Res Lett 35:2008GL034864. https://doi.org/10.1029/2008GL034864

Lee T, Fukumori I, Tang B (2004) Temperature advection: internal versus external processes. J Phys Oceanogr 34:1936–1944. https://doi.org/10.1175/1520-0485(2004)034%3c1936:TAIVEP%3e2.0.CO;2

Lee T, Fournier S, Gordon AL, Sprintall J (2019) Maritime continent water cycle regulates low-latitude chokepoint of global ocean circulation. Nat Commun 10:1–13. https://doi.org/10.1038/s41467-019-10109-z

Li Y, Chen Q, Liu X et al (2019) Long-Term trend of the tropical pacific trade winds under global warming and its causes. J Geophy Res Oceans 124:2626–2640. https://doi.org/10.1029/2018JC014603

Liang L, Xue H, Shu Y (2019) The Indonesian throughflow and the circulation in the Banda sea: a modeling study. J Geophys Res Oceans 124:3089–3106. https://doi.org/10.1029/2018JC014926

Liu L, Yang G, Zhao X et al (2017) Why was the Indian ocean dipole weak in the context of the extreme El Niño in 2015? J Climate 30:4755–4761. https://doi.org/10.1175/JCLI-D-16-0281.1

Maher N, England MH, Gupta AS, Spence P (2018) Role of Pacific trade winds in driving ocean temperatures during the recent slowdown and projections under a wind trend reversal. Clim Dyn 51:321–336. https://doi.org/10.1007/s00382-017-3923-3

Marchesiello P, McWilliams JC, Shchepetkin A (2001) Open boundary conditions for long-term integration of regional oceanic models. Ocean Model 3:1–20. https://doi.org/10.1016/S1463-5003(00)00013-5

Mayer M, Alonso Balmaseda M, Haimberger L (2018) Unprecedented 2015/2016 Indo-Pacific heat transfer speeds up tropical pacific heat recharge. Geophys Res Lett 45:3274–3284. https://doi.org/10.1002/2018GL077106

McBride JL, Haylock MR, Nicholls N (2003) Relationships between the maritime continent heat source and the El Niño-southern oscillation phenomenon. J Clim 16:2905–2914. https://doi.org/10.1175/1520-0442(2003)016%3c2905:RBTMCH%3e2.0.CO;2

Meehl GA, Lukas R, Kiladis GN et al (2001) A conceptual framework for time and space scale interactions in the climate system. Clim Dyn 17:753–775. https://doi.org/10.1007/s003820000143

Meehl GA, Teng H, Capotondi A, Hu A (2021) The role of interannual ENSO events in decadal timescale transitions of the interdecadal Pacific oscillation. Clim Dyn 57:1933–1951. https://doi.org/10.1007/s00382-021-05784-y

Mellor GL, Yamada T (1982) Development of a turbulence closure model for geophysical fluid problems. Rev Geophys 20:851. https://doi.org/10.1029/RG020i004p00851

Moltmann T, Turton J, Zhang H-M et al (2019) A global ocean observing system (GOOS), delivered through enhanced collaboration across regions, communities, and new technologies. Front Mar Sci 6:291. https://doi.org/10.3389/fmars.2019.00291

Moreton SM, Ferreira D, Roberts MJ, Hewitt HT (2020) Evaluating surface eddy properties in coupled climate simulations with 'eddy-present' and 'eddy-rich' ocean resolution. Ocean Model 147:101567. https://doi.org/10.1016/j.ocemod.2020.101567

Murata K, Kido S, Tozuka T (2020) Role of reemergence in the central north Pacific revealed by a mixed layer heat budget analysis. Geophys Res Lett. https://doi.org/10.1029/2020GL088194

Ng B, Cai W, Walsh K (2014) The role of the SST-thermocline relationship in Indian ocean dipole skewness and its response to global warming. Sci Rep 4:6034. https://doi.org/10.1038/srep06034

Ningsih NS, Rakhmaputeri N, Harto AB (2013) Upwelling variability along the southern coast of Bali and in Nusa Tenggara waters. Ocean Sci J 48:49–57. https://doi.org/10.1007/s12601-013-0004-3

Pujiana K, McPhaden MJ, Gordon AL, Napitu AM (2019) Unprecedented response of Indonesian throughflow to anomalous Indo-Pacific climatic forcing in 2016. J Geophys Res Oceans 124:3737–3754. https://doi.org/10.1029/2018JC014574

Ramos CGM, Tan H, Ray P, Dudhia J (2022) Estimates of the sensible heat of rainfall in the tropics from reanalysis and observations. Intl J Climatol 42:2246–2259. https://doi.org/10.1002/joc.7363

Rayner NA, Parker DE, Horton EB et al (2003) Global analyses of sea surface temperature, sea ice, and night marine air temperature since the late nineteenth century. J Geophys Res Atmos. https://doi.org/10.1029/2002jd002670

Saji NH, Goswami PN, Vinayachandran PN, Yamagata T (1999) A dipole mode in the tropical Indian Ocean. Nature 401:360–363

Saji NH, Yamagata T (2003) Possible impacts of Indian ocean dipole mode events on global climate. Climate Res 25:151–169. https://doi.org/10.3354/cr025151

Sánchez-Román A, Pujol MI, Faugère Y, Pascual A (2023) DUACS DT2021 reprocessed altimetry improves sea level retrieval in the coastal band of the European seas. Ocean Sci 19:793–809. https://doi.org/10.5194/os-19-793-2023

Shchepetkin AF, McWilliams JC (2005) The regional oceanic modeling system (ROMS): a split-explicit, free-surface, topography-following-coordinate oceanic model. Ocean Model 9:347–404. https://doi.org/10.1016/j.ocemod.2004.08.002

Song Y, Haidvogel D (1994) A semi-implicit ocean circulation model using a generalized topography-following coordinate system. J Comput Phys 115:228–244. https://doi.org/10.1006/jcph.1994.1189

Sprintall J, Wijffels SE, Molcard R, Jaya I (2009) Direct estimates of the indonesian throughflow entering the Indian ocean: 2004–2006. J Geophys Res Oceans 114:2004–2006. https://doi.org/10.1029/2008JC005257

Sprintall J, Gordon AL, Wijffels SE et al (2019) Detecting change in the Indonesian seas. Front Mar Sci. https://doi.org/10.3389/fmars.2019.00257

Sun C, Kucharski F, Li J et al (2017) Western tropical Pacific multidecadal variability forced by the Atlantic multidecadal

oscillation. Nat Commun 8:1–10. https://doi.org/10.1038/ncomms15998
Suzuki T, Yamazaki D, Tsujino H et al (2018) A dataset of continental river discharge based on JRA-55 for use in a global ocean circulation model. J Oceanogr 74:421–429. https://doi.org/10.1007/s10872-017-0458-5
Thirumalai K, DiNezio PN, Okumura Y, Deser C (2017) Extreme temperatures in southeast Asia caused by El Niño and worsened by global warming. Nat Commun 8:15531. https://doi.org/10.1038/ncomms15531
Timmermann A, An SI, Kug JS et al (2018) El Niño–Southern Oscillation complexity. Nature 559:535–545. https://doi.org/10.1038/s41586-018-0252-6
Tomita H, Hihara T, Kako S et al (2019) An introduction to J-OFURO3, a third-generation Japanese ocean flux data set using remote-sensing observations. J Oceanogr 75:171–194. https://doi.org/10.1007/s10872-018-0493-x
Trenberth KE (1997) The definition of El Niño. Bull Am Meteor Soc 78:2771–2777. https://doi.org/10.1175/1520-0477(1997)078%3c2771:TDOENO%3e2.0.CO;2
Trenberth KE, Caron JM, Stepaniak DP, Worley S (2002) Evolution of El Niño-Southern Oscillation and global atmospheric surface temperatures. J Geophys Res. https://doi.org/10.1029/2000JD000298
Tsujino H, Urakawa S, Nakano H et al (2018) JRA-55 based surface dataset for driving ocean–sea-ice models (JRA55-do). Ocean Model 130:79–139. https://doi.org/10.1016/j.ocemod.2018.07.002
Tsujino H, Urakawa LS, Griffies SM et al (2020) Evaluation of global ocean–sea-ice model simulations based on the experimental protocols of the ocean model intercomparison project phase 2 (OMIP-2). Geosci Model Dev 13:3643–3708. https://doi.org/10.5194/gmd-13-3643-2020
Wang W, McPhaden MJ (2000) The Surface-layer heat balance in the equatorial pacific ocean. Part II: interannual variability*. J Phys Oceanogr 30:2989–3008. https://doi.org/10.1175/1520-0485(2001)031%3c2989:TSLHBI%3e2.0.CO;2
Wang C, Enfield DB (2001) The tropical western hemisphere warm pool. Geophys Res Lett 28:1635–1638. https://doi.org/10.1029/2000GL011763
Wijffels S, Meyers G (2004) An intersection of oceanic waveguides: variability in the Indonesian throughflow region. J Phys Oceanogr 34:1232–1253. https://doi.org/10.1175/1520-0485(2004)034%3c1232:AIOOWV%3e2.0.CO;2
Wilkin JL (2006) The summertime heat budget and circulation of southeast New England shelf waters. J Phys Oceanogr 36:1997–2011. https://doi.org/10.1175/JPO2968.1
Zhang GJ, Mcphaden MJ (1995) The relationship between sea surface temperature and latent heat flux in the equatorial Pacific. J Climate 8:589–605. https://doi.org/10.1175/1520-0442(1995)008%3c0589:TRBSST%3e2.0.CO;2
Zhang Y, Feng M, Du Y et al (2018) Strengthened Indonesian throughflow drives decadal warming in the southern Indian ocean. Geophys Res Lett 45:6167–6175. https://doi.org/10.1029/2018GL078265
Zhang T, Hoell A, Perlwitz J et al (2019) Towards probabilistic multivariate ENSO monitoring. Geophys Res Lett 46:10532–10540. https://doi.org/10.1029/2019GL083946
Zuo H, Balmaseda MA, Tietsche S et al (2019) The ECMWF operational ensemble reanalysis-analysis system for ocean and sea ice: a description of the system and assessment. Ocean Sci 15:779–808. https://doi.org/10.5194/os-15-779-2019
Zweng MM, Reagan JR, Seidov D, Boyer TP, Locarnini RA, Garcia HE, Mishonov AV, Baranova OK, Weathers K, Paver CR, Smolyar I (2018) World Ocean Atlas 2018, Volume 2: Salinity. NOAA Atlas NESDIS 82, 50pp. https://www.ncei.noaa.gov/access/world-ocean-atlas-2018/